University of Naples Federico II

School of Polytechnic Basic Sciences

*Department of Chemical, Materials and Industrial Production Engineering*

Ph.D. in Industrial Products and Processes Engineering - XXXVI Cycle


Ph.D. Thesis

# Enhancing Fatigue Performance of Additively Manufactured Ti6Al4V Components through tool-less treatments: Chemical Machining and Laser Polishing

**Tutor Ph.D.**
Antonino Squillace

**Candidate**
Emanuele Manco

## Abstract

Additive manufacturing (AM) processes, while revolutionary, encounter various hurdles, for example, metals processed via AM technologies are prone to internal defects, leading to suboptimal mechanical properties.

Surface quality poses a considerable challenge to the stable implementation of AM. High surface roughness, particularly prevalent in AM-processed metals, compromises fatigue behavior, tribological properties and corrosion resistance properties. Additionally, surface roughness values vary significantly depending on the specific AM technology employed.

Many articles in the literature compare the fatigue properties of additively manufactured as-built samples to additively manufactured turned samples to emphasize the role of surface quality. While these comparisons provide a valuable benchmark, it's important to note that turning, although effective in achieving low roughness values, may not align with the design flexibility offered by additive manufacturing. Consequently, there is a growing interest in exploring tool-less surface treatments for enhancing surface quality in additive manufacturing. While some studies exist, they often focus on simple geometries and lack evaluation of their impact on fatigue properties.

For this research, the rotating beam fatigue testing method has been preferred over any other fatigue testing method because during tests, the most stressed points are always on the surface in order to highlight the effectiveness of surface treatments.

This work aims to develop, investigate and analyze tool-less surface treatments (chemical machining and laser polishing) that can enhance the surface quality of additively manufactured Ti6Al4V and validate the influence of the treatment in terms of fatigue properties in the parts.

# Introduction

## Additive manufacturing for metal parts

Additive Manufacturing (AM), often referred to as 3D printing, has revolutionized the manufacturing industry by offering innovative solutions to fabricate complex and customized metal components. Unlike traditional subtractive manufacturing processes, such as milling or machining, which involve cutting away material from a solid block, AM builds objects layer by layer from digital designs. This groundbreaking technology has gained significant prominence over the past few decades, especially in the field of metal production [1].

*Figure 1 Additively manufactured parts realized utilizing Powder Bed Fusion. (https://www.flickr.com/photos/oakridgelab/9067742195/in/photostream/)*

The concept of additive manufacturing can be traced back to the 1980s when the first experiments in layer-by-layer construction were conducted. However, it is in recent years that metal additive manufacturing has truly come into its own, enabling the production of functional, high-performance parts with previously unattainable geometries and material properties.

One of the primary driving forces behind the widespread adoption of metal AM is its ability to overcome the limitations of conventional manufacturing techniques. It offers unparalleled design freedom, allowing engineers to create intricate structures and shapes that were once impractical or impossible to achieve. This flexibility is particularly valuable in industries where lightweight, highly customized, or complex geometries are crucial, such as aerospace, automotive, medical, and even jewelry.

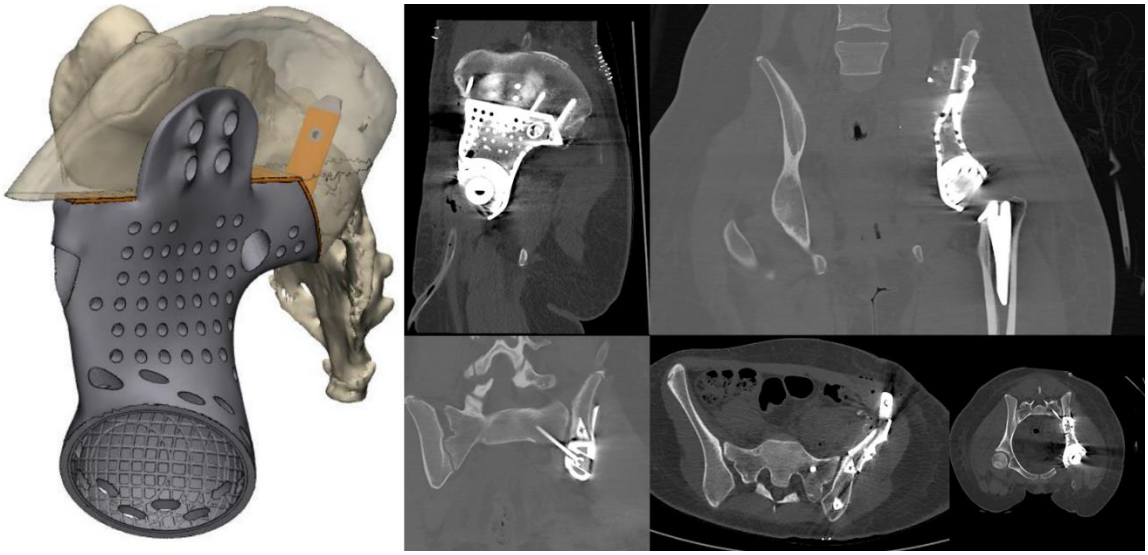

*Figure 2 Custom additively manufactured protheses. (https://www.ge.com/additive/press-releases/mt-ortho-harnesses-additive-technology-manufacture-customized-prostheses)*

In metal additive manufacturing, a range of materials can be utilized, with metals like titanium, aluminum, stainless steel, and nickel-based alloys being some of the most common choices. Each material brings its own set of properties, from exceptional strength and heat resistance to corrosion resistance, making metal AM suitable for an extensive array of applications.

These advantages are particularly pronounced when utilizing powders as the feedstock in Additive Manufacturing (AM). This is due to their versatility in localized manipulation and minimal material waste, especially when compared to various feedstocks used in traditional manufacturing processes.

To provide a comprehensive overview of the state of the art in metal AM processes, several authors have presented review papers for clear descriptions [2, 3]. However, the spectrum of actual processes can be categorized based on:

- The type of feedstock used as the raw material.
- The external heat source employed for material melting is an essential step to achieve the desired final shape through layer-wise solidification.
- The systems used for material displacement and consolidation.

Based on these criteria, metal Additive Manufacturing (AM) technologies can be broadly categorized into two primary classes: Powder Bed Fusion (PBF) and Directed Energy Deposition (DED) processes. The latter encompasses both powders and wires as potential feedstock materials.

In PBF processes, the raw material is initially stored in a feeding tank and then evenly distributed across a building platform using a roller, often referred to as a recoated blade. Once the powder bed covers the entire platform area, its thickness is predetermined based on design considerations and particle size. Selective melting of the powders is then achieved using a focused heat source, leading to consolidation upon cooling, forming a single section of the final part. This process is repeated as the building platform is incrementally lowered along the vertical axis, adhering to the common layer-by-layer approach characteristic of all AM processes.

The choice of the specific heat source in PBF processes depends on the materials processed and their intended applications. It leads to the classification of PBF processes into two main groups: Selective Laser Melting (SLM) and Electron Beam Melting (EBM) [4].

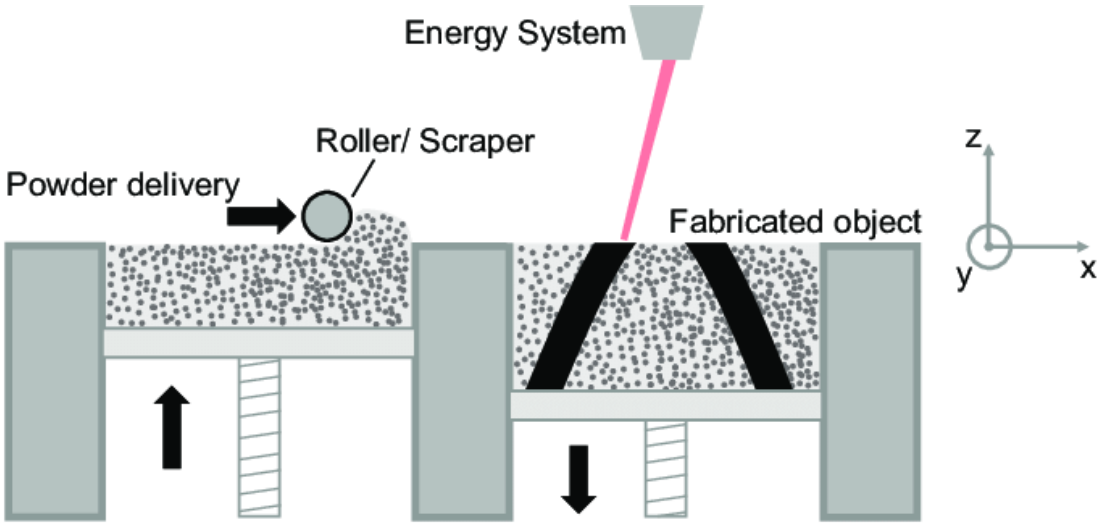


*Figure 3 Overview of powder bed fusion additive manufacturing technology* [5].

SLM and EBM exhibit notable differences in terms of machine construction, the materials they typically process, and the applications for which the final parts are intended [6]. For instance, EBM can accommodate thicker layers compared to SLM due to the greater penetrating power of the electron beam compared to lasers [7]. This results in higher production rates, influenced by scanning speed. Controlling scanning speed is more challenging in EBM due to the electron beam's operational principles, and EBM machines use speed functions for this purpose [8]. These speed functions are specialized algorithms implemented by EBM machine manufacturers to optimize energy input distribution within different layers and build heights, based on extensive process parameter optimization for specific materials. Similar considerations regarding default process parameters can be made for SLM machines. Another distinction between EBM and SLM lies in the process chamber conditions. EBM machines typically preheat the building platform to minimize temperature gradients, a major cause of residual stresses and part distortion[9]. This is achieved by employing defocused electron beam parameters directly on the platform to raise the temperature. Such a practice is not consistently found or applied in SLM. Additionally, EBM, due to its need for electron beam stability, requires operating under vacuum [10], whereas SLM commonly uses inert gases like Argon or Nitrogen to prevent oxidation of processed metal powders. Nevertheless, vacuum conditions and building platform preheating in EBM ensure high-quality parts, on par with or superior to SLM-produced parts.

In the realm of metal AM, with a specific focus on EBM and SLM processes, surface quality is an essential consideration. Since any interaction between parts and their environment occurs through their surfaces, surface characteristics significantly affect functionality. This applies to engineering, where surface characteristics are crucial in explaining a part's behavior concerning properties such as wettability, corrosion, wear, reflectivity, and more [11]. These considerations are equally valid for AM products.

Across the entire spectrum of AM technologies, the surface quality of produced parts is greatly influenced by specific process parameters. Two key factors affecting surface characteristics are layer thickness and part orientation relative to the building platform [12]. The layer thickness, constrained by the size of the feedstock's minimum and maximum values determined by melt pool depth, can be adjusted to accelerate the build rate and leverage AM's design flexibility. However, this choice can result in poorer surface quality on curved surfaces due to the "stair-step effect," where free-form surfaces are approximated

by stacking material layers of a defined height. A thicker layer exacerbates this effect [13], impacting surface roughness. Additionally, surface quality in PBF metal AM parts can be compromised due to two other factors [14]:

- Lack of fusion of processed powders, typically caused by incorrect process parameters related to the heat source, such as insufficient power and excessively high scanning speed.
- The "balling effect," a complex phenomenon related to melt pool dynamics: when the scanning speed is too high, the melt pool becomes elongated and unstable, leading to break-up into multiple shorter tracks.

Therefore, considering the combination of the mentioned phenomena, the surfaces of L-PBF parts are characterized by a random and sintered powders-rich texture that leads to unacceptable roughness making a post-process surface finishing step essential to obtain parts that are satisfactory for the end applications.

## Applications and constraints

The influence of metal additive manufacturing (AM) extends well beyond biomedical, aerospace and automotive sectors, permeating various other domains and showcasing its adaptability in addressing unique challenges. In the energy sector, for instance, the technology has found application in the development of highly efficient heat exchangers, which are vital for optimizing energy transfer processes in power generation and industrial applications. The intricate geometries achievable through metal AM enable the design of heat exchangers with enhanced thermal performance, reduced energy consumption, and minimized environmental impact.

Moreover, the drive for sustainable energy sources has led to the use of metal AM in the production of components for renewable energy systems. Turbine components, such as blades and vanes, benefit from AM's design flexibility and precision, resulting in more efficient and durable wind turbines and gas turbines. These advancements not only contribute to a cleaner environment but also improve the overall reliability and longevity of energy infrastructure.

In the realm of luxury and high-end craftsmanship, metal AM has made waves in the jewelry industry. The technology's ability to create intricate and personalized designs has unlocked new creative avenues for jewelry designers and manufacturers. From bespoke

engagement rings to avant-garde statement pieces, metal AM empowers artisans to push the boundaries of design, all while working with precious metals like gold and platinum. This fusion of traditional craftsmanship with cutting-edge technology has redefined the jewelry landscape, offering consumers a unique and personalized experience.

In summary, AM capacity to produce complex, lightweight, and customized components is revolutionizing manufacturing processes and driving innovation across sectors. As technology continues to evolve, the potential for even more groundbreaking applications in these and other fields remains on the horizon, solidifying metal AM as a transformative force in modern industry.

However, to achieve a comprehensive understanding of AM, it is imperative to address its drawbacks and limitations within the current state of the art. The main challenges are resumed following:

*Limited Number of Available Materials*

This constraint is related to the requirement for a thorough grasp of processes. AM technologies include a higher number of adjustable process factors than traditional production processes, needing substantial study to discover ideal conditions for each material. Fortunately, the development and implementation of rigorous experimental methodologies based on statistical models has accelerated the examination of integrated process parameters.

*Surface Quality*

Surface quality is a significant barrier to the successful application of AM. High surface roughness, which is especially common in AM-processed metals, degrades mechanical, tribological, and corrosion resistance qualities. Furthermore, surface roughness levels vary greatly depending on the AM method used.

*Limited Building Volumes*

Metal AM procedures, particularly powder-based approaches, are limited in terms of construction volume. Building volumes for powder bed fusion (PBF) AM techniques seldom reach 500 x 500 x 500 $mm^3$ in general. Given the reactivity of metal powder during melting, this constraint is mostly related to the necessity for precise environmental control in procedures such as Selective Laser Melting (SLM) and Electron Beam Melting (EBM).

Larger quantities result in lower productivity and higher equipment costs, motivating the desire for concurrent manufacture of sub-parts that may be assembled later.

*Low Dimensional Accuracy*

Shrinkage concerns, residual stress generation during AM material processing, the resolution of certain AM machines, and component orientation on building platforms all restrict dimensional accuracy.

*Low Productivity*

Part complexity is inextricably linked to the productivity of the additive manufacturing process. In terms of component dimensions, AM methods are often less productive than standard CNC machining. Productivity is also affected by process parameter selection, design considerations, and the demand for pre- and post-processing processes to suit specific application requirements.

*Pre and post processing*

While AM techniques are near-net-shape technologies, they are not stand-alone operations. To complete the AM manufacturing process, several pre- and post-processing procedures are required. Post-processing surface finishing operations, for example, are required to remove supports utilized during component construction and obtain the appropriate surface quality. Furthermore, powder management activities, such as processes for reusing powders in successive AM builds, provide additional complications. Adoption of new metrology and characterization standards is also required to achieve the desired quality of final goods.

Given the cumulative impact of the above-listed obstacles, it is clear that the seamless integration of AM technologies remains a long way off. These difficulties also have an impact on the cost assessment and modeling related to the implementation of AM technology. When viable, the costs associated with AM methods are currently greater than those connected with traditional manufacturing procedures. Some researchers have attempted to develop cost models for additive manufacturing that take into account both main structured costs (e.g., machines, materials, labor) and incidental structured costs (e.g., idle times, mistake prevention, and failure costs). However, given the length of the AM value chain, attaining reliable industry integration remains a significant challenge.

To summarize, additive manufacturing, while promising, confronts several problems in terms of methods, materials, and surface quality.

This work aims to investigate the surface quality issue, analyzing two different surface finishing methods, and measuring their impact on fatigue performance.

## Surface finishing methods for Additive Manufacturing

Additive Manufacturing (AM), has revolutionized the manufacturing industry by offering innovative solutions to fabricate complex and customized metal components. Unlike traditional subtractive manufacturing processes, AM builds objects layer by layer from digital designs. This groundbreaking technology has gained significant prominence over the past few decades, especially in the field of metal production.

AM processes, however, are characterized by several problems, as discussed in the previous chapter, leading to suboptimal mechanical properties.

Surface quality poses a considerable challenge to the stable implementation of AM. High surface roughness, particularly prevalent in AM-processed metals, compromises fatigue behavior, tribological properties and corrosion resistance properties. Additionally, surface roughness values vary significantly depending on the specific AM technology employed.

Many articles in the literature compare the fatigue properties of additively manufactured as-built samples to additively manufactured turned samples to emphasize the role of surface quality. While these comparisons provide a valuable benchmark, it's important to note that turning, although effective in achieving low roughness values, may not align with the design flexibility offered by additive manufacturing. Consequently, there is a growing interest in exploring tool-less surface treatments for enhancing surface quality in additive manufacturing

According to the current state of the art, there are several methods for surface post processing of metal AM components, regardless of the method, they can be classified according to their type of interaction with the parts, such as mechanical, thermal, chemical/electrochemical, or a mixture of these.

Mechanical contact treatments are the most used methods, but they are not suitable for complex geometries typical of AM parts. CNC machining [15], shot peening [16, 17], vibratory polishing, and sandblasting [18] are the most common processes in this category.

Given the challenging and complex properties of AM metal components, various methods used in other fields are an attractive topic for surface treatment. Fluidized bed and hydrodynamic cavitation grinding techniques are two examples [19–21]. Except for the latter techniques, mechanically based surface treatments have significant limitations in terms of physical access of tools and abrasives to complex shaped components that can be

achieved by AM. The same can be said for surface treatments based on thermal interaction. This area is primarily concerned with laser polishing, a process based on surface remelting. Laser polishing provides better process control than other methods because the characteristics of the laser source are accurate and process parameters, for example, laser power, scan speed, overlap between tracks, etc., can be easily regulated. This feature is highly desirable for a smoothing technique applied to a surface with random texture, such as that produced by AM processes, however, as with various mechanical treatments, the application of laser polishing is hindered by the need for physical access of the laser beam to intricate internal structures, and for this reason, the number of possible applications is limited.

Given these assumptions, numerous authors [22–24] have studied laser polishing performance for different materials. Examples of this may be seen in Obeidi et al research on laser polishing, which shows that the surface roughness of Ti6Al4V specimens generated by laser powder bed fusion can be decreased from the initial value by up to 90% [25] (final Sa of 3 μm for both flat and cylindrical specimens). Researchers have extensively studied the effects of laser polishing on the surface quality of metal AM parts, particularly for L-PBF processes, utilizing NdYAG and Yb fiber lasers. While fiber lasers are commonly used due to their absorption properties, recent research has explored the use of pulsed lasers with ultrashort pulse durations for enhanced radiation absorption and retention of microstructure features [26, 27]. It is worth noting that laser absorption mechanisms depend not only on the material but also on the surface roughness, with roughness-induced absorption enhancement potentially enabling the use of CO2 lasers for polishing highly reflective materials [28].

Laser polishing is one such process, which offers precise control of process parameters, high process automation, high surface quality, and superficial microstructure refinement that enhances properties such as corrosion and wear resistance without creating pores, cracks, or hidden surface defects, and without affecting the component size after treatment [29].

Chemical surface treatments, on the other hand, remain one of the most promising methods for homogeneous smoothing of complex parts and surfaces, such as lattice structures. The fundamental perk of chemical treatments relies on the mobility of ions in aggressive solutions, which can be precisely regulated and enhanced when controlled by an electric potential. Scherillo et al studied the chemical polishing on AlSi10Mg specimens fabricated by SLM and Ti6Al4V fabricated by EBM with a simple geometry and found a significant

improvement in surface quality as measured by various indicators [1, 30]. In addition, Wysocki et al [31] demonstrated the efficacy of chemical processing in improving the surface quality of Ti6Al4V scaffolds fabricated by EBM and the ability of the treatment to integrate bone cells.

## Fatigue testing of additively manufactured parts

Fatigue testing of additively manufactured metal pieces has shown a wide variety of results for many investigators. Categorizing the results based on the conditions of built pieces can help summarize the state of the art of fatigue testing for additively manufactured parts. The categorization proposed is:

- General flaws;
- Microstructure flaws;
- Surface flaws.

While general flaws (such as lack of fusion and pores) can be avoided with the optimization of the deposition method or HIPing [32, 33] and microstructure can be controlled by heat treatments, post process surface finishing treatments are generally necessary to improve surface quality.

When failure strongly depends on surface flaws, both heat treatment and HIP will have a more limited effect in this case. A comparison between different treatments is provided by Fatemi et al. [34] review. To sum up, the most investigated contributions to fatigue life are:

- Effects of surface treatments;
- Effects of the direction of loading;
- Effects of heat treatments.

Another conclusion enucleated from literature studies is rotating-beam fatigue test is considered being the best test if surface quality influence is intended to be investigated. Manson et al. [35] demonstrated that the difference in surface strain in the axial and rotating bending tests is a reason for the difference in the fatigue lives from these two tests.

In rotating bending, cantilever, and four-point bending tests, the stress gradients are the same if the same size specimens are used (figure 4). However, in rotating bending tests all the points on the surface of the pipe specimens are subjected to maximum stress. A comparison of the test data shows that, in the low-cycle range, the rotating bending test yields a lower fatigue strength than the cantilever and four-point bending tests.

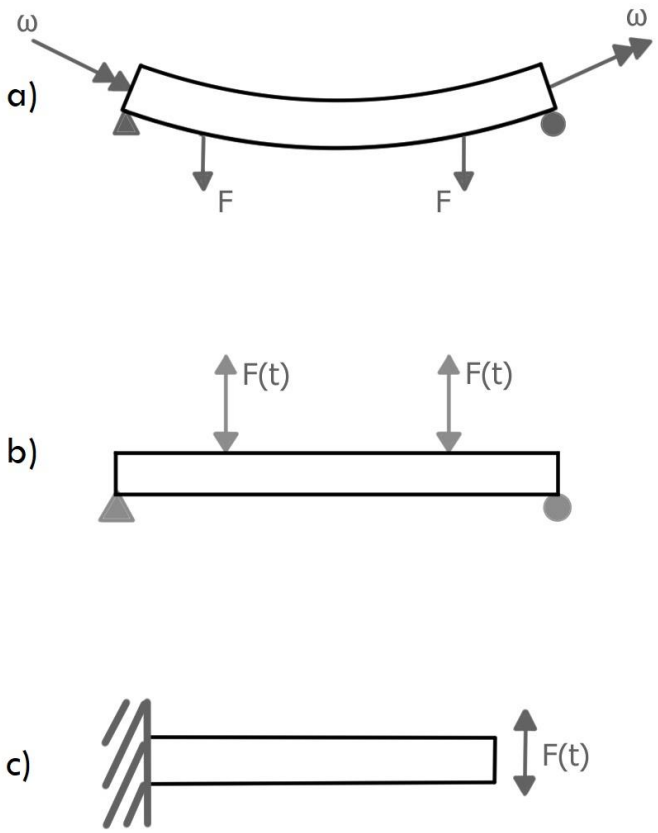


*Figure 4: a) rotating beam fatigue testing scheme, b) four point fatigue testing scheme, c) cantilever fatigue testing scheme.*

RBF testing is strategically chosen to delve into the intricate relationship between surface quality and fatigue behavior within various components because the testing method focuses on the most stressed portion of the specimen's surface, providing insights into fatigue contributions. In bending fatigue testing the surface is subjected to, maximum stress, thus cracks are expected to nucleate from the surface. The rotating beam fatigue test is generally characterized by lower resistance to fatigue failure if compared to other bending tests because the entire surface is subjected to maximum stress.

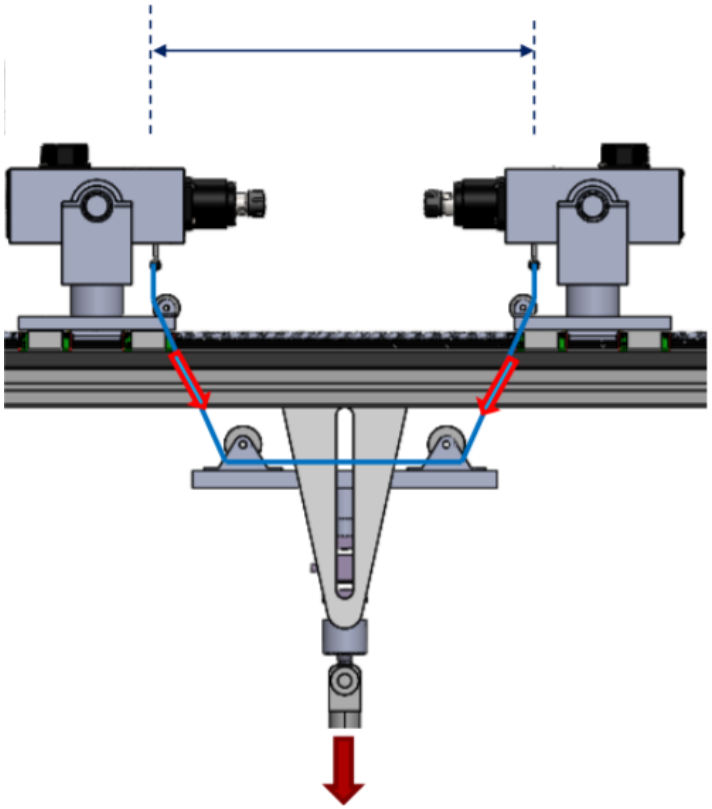

*Figure 5 Rotating Beam Fatigue testing machine scheme.*

The possibility to 3D print titanium alloys creates new opportunities for designing and manufacturing of load carrying components [34], but fatigue behaviour needs to be further investigated [36, 37]. Most studies [38, 39] are based on the investigation of the build direction influence on fatigue performance, some researchers focus attention on the influence of beneficial heat treatments to reduce the dimensions of internal defects [40, 41]. Regarding surface modification treatments [34], researchers in literature have extensively investigated the impact of machining while there's a considerable gap of knowledge the fatigue behaviour of additively manufactured parts after tool-less treatments, especially chemical finishing.

Despite the number of papers regarding surface treatments and fatigue testing, most of the works investigated the influence of mechanical machining on the fatigue life, while chemical finishing and laser polishing study is still open. This thesis aims to provide further data for surface finishing treatments and to correlate surface finishing results with fatigue behavior.

## Chemical Finishing

In this section, the study conducted on chemical surface finishing for Ti6Al4V is discussed in detail, starting with the preliminary analysis of the chemical solutions for simple geometries, followed by treatment optimization for cylindrical shapes for dogbone samples. The final part of the chapter investigates the impact on fatigue behavior of the chemical treatment.

The study utilized samples that were produced by commencing with powder of a titanium Ti6Al4V grade 5 alloy, exhibiting a spherical morphology. Table 1 details the composition of the powders, with particle sizes falling within the range of 45-106 µm.

| Element | wt% |
|---|---|
| **Al** | 6.40 |
| **V** | 4.12 |
| **Fe** | 0.18 |
| **O** | 0.14 |
| **N** | 0.01 |
| **H** | 0.003 |
| **C** | 0.01 |
| **Ti** | Balance |

*Table 1: Composition of Ti6Al4V powders*

The EBM machine used for this study is an ARCAM A2X, and the software installed was the EBM Control version 3.2. The whole process takes place in a vacuum, the pressure of the building volume being about 10-4 mbar. The specimens manufactured have been built by using standard Ti6Al4V melt themes for a layer thickness of 50 µm. This build theme varies electron beam parameters in a controlled sequence throughout the build according to algorithms developed by the manufacturer. In this algorithm, the beam current and the beam speed continuously change but the energy density of the process is kept constant at the value of 40 J/mm3 to maximize the density of the component with a line offset of 0.1 mm. The orientation and the location of the samples in the build chamber were set by using the Materialize Magics software. As the specimens were grown directly on the start plate,

wafer supports aimed at dissipating the heat generated by the electron beam were not used. All the specimens were scaled according to the ARCAM recommended scale factors (1.0092 for x and y direction and 1.0132 for z direction) in order to take into account the thermal shrinkage occurring after the melting. The orientation of the sample implies that the stair-case effect has little influence on the final quality of the surface and depends mainly on the lack of fusion and balling effect.

## Planar geometry case

Experimental tests were performed on samples obtained from parallelepiped manufactured in EBM and with the geometry and dimensions shown in Figure 6.

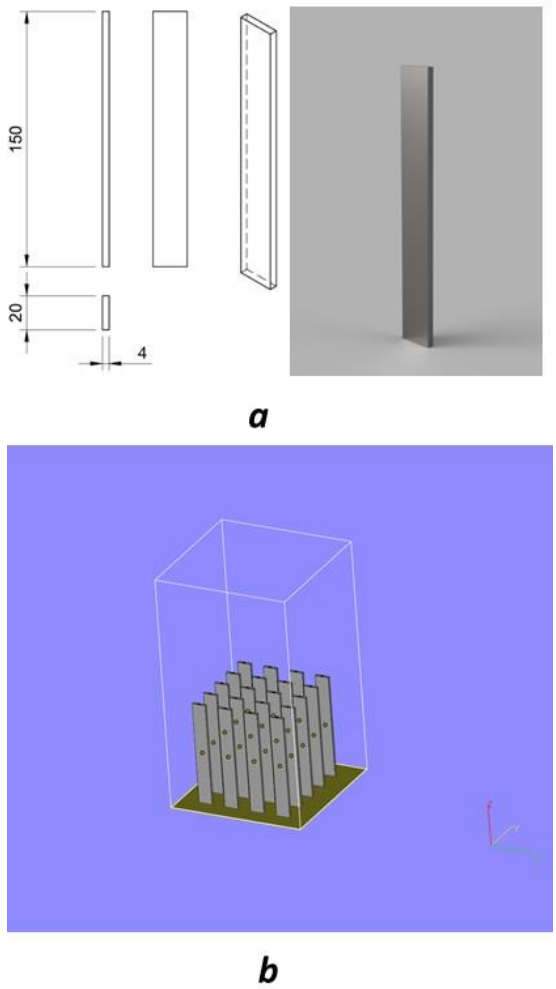


*Figure 6: (a) dimension in mm and picture of the specimen and (b) orientation of specimen employed in the experiments.*

The specimens subjected to chemical smoothing were cut from the parallelepipeds described above and squared samples of 20X20 mm were mounted in a sample holder and immersed in the acidic solutions according to the scheme reported in Figure 2, furthermore, no contour strategy has been adopted meaning that the initial quality of the surface is the worst possible. This choice has been made to fully exploit the capabilities of the process; moreover, according to Beevers et al [42], the contour strategy causes a significant decrease in the fatigue resistance of the material.

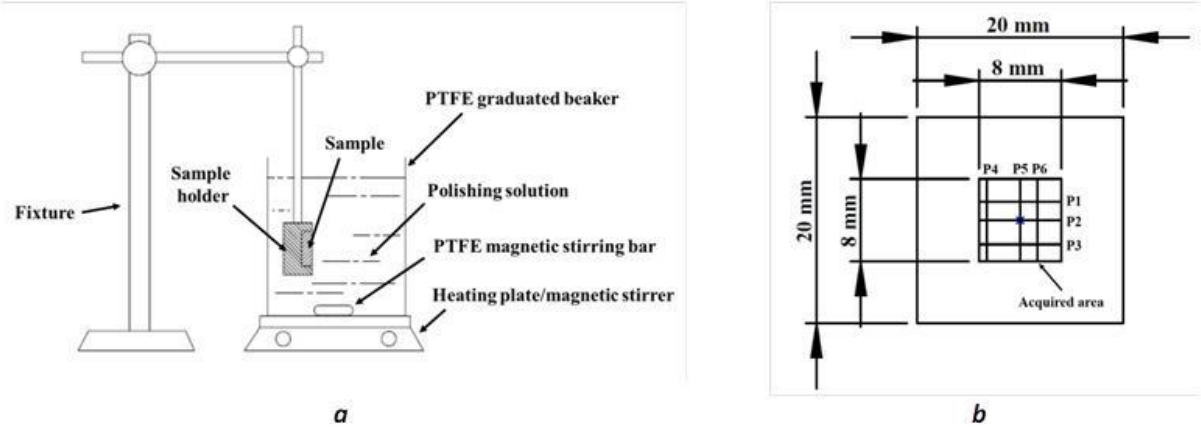


*Figure 7: (a) Setup of the experiment; (b) dimension of samples and acquired area and profiles.*

In order to verify the influence of the ratio $HF/HNO_3$ on the smoothing capabilities of the process, four different solutions were prepared whose composition is given in Table 2.
Even if chemical machining is a well-developed process to work titanium components, the composition of the solution is often based upon empirical considerations. The $HF/HNO_3$ ratio of the solutions employed in this work is the one commonly used in practice.
The evolution of the process has been studied by analyzing the surface and measuring the weight of the samples at regular intervals. To this aim, every 20 minutes the samples were taken out from the solution, rinsed in distilled water, and ultrasonic cleaned in distilled water for 15 minutes. After that, the surface parameters were acquired using a Leica DCM 3D confocal microscope. The parameters used to characterize the surface were Sa, Sz, and Pdq. Sa represents the average of the absolute value of all peaks and valleys with respect to the median plane, Sz is the sum of the largest peak height value and the largest pit depth value within the defined area, Pdq is a measure of the slope of peaks and valleys, values of

Pdq near zero indicating a flat surface [43]. The surface parameters are relative to the primary surface and calculated by means of the Leica Map software according to BS EN ISO 25178-2 and BS EN ISO 4287. The values reported in the result session are the average of measurements made on five different samples. For every sample, a small area of 8X8 mm2 has been measured in the center (see figure 7b).

From the weight of the sample the Etching Rate (ER) has been calculated, being ER defined as:

$$ER = \frac{w_{i-1} - w_i}{t_i - t_{i-1}} \cdot \frac{1}{A}$$

where $w_i$ and $w_{i-1}$ are the weight of the sample at time $t_i$ and $t_{i-1}$ respectively; five samples have been used for every solution. Other information about the process has been collected utilizing a Scanning Electron Microscope (SEM) coupled with Energy Dispersion X-Ray analysis (EDX). To this aim, the surface of the samples after rinsing and ultrasonic cleaning were analyzed using a Hitachi TM 3000 microscope coupled with an Oxford Instrument Swift ED3000 EDX probe.

| | **H2O, ml** | **HNO3 (69 wt%), ml** | **HF (48 wt%), ml** | **HF/HNO3 molar ratio** |
|---|---|---|---|---|
| **Sol. 1** | 537 | 164 | 28 | 0.3 |
| **Sol. 2** | 653 | 82 | 28 | 0.6 |
| **Sol. 3** | 695 | 52 | 28 | 1 |
| **Sol. 4** | 768 | 0 | 28 | |

*Table 2: composition of acidic solution employed in the treatment.*

The dissolution of titanium in a solution containing HF occurs with an electrochemical mechanism according to the following semi-reactions [44, 45]:

Anodic:

$Ti \rightarrow Ti^{3+} + 3e^-$ (1)

$Ti^{3+} + 6HF \rightarrow [TiF_6]^{2-} + 6H^+ + e^-$ (2)

And cathodic:

$4H^+ + 4e^- \rightarrow 2H_2$ (3)

The complexed ion $[TiF_6]^{2-}$ is soluble and the hydrogen produced in reaction (3) is gaseous. In competition with reaction (2) titanium dioxide is produced according to:

$Ti^{3+} + 2H_2O \rightarrow TiO_2 + 4H^+ + e^-$

(4)

However, the oxidative power of $H_2O$ is too low to produce a significant amount of $TiO_2$, and in solutions containing only HF the dissolution of titanium occurs via reactions (1) e (2).

In presence of $HNO_3$, a strong oxidizing agent, $TiO_2$ is produced according to the reactions:

$Ti^{3+} + 1/2HNO_3 + 3/2H_2O \rightarrow TiO_2 + 1/2HNO_2 + 3H^+$

(5)

$TiO_2$ reacts with HF to produce soluble $[TiF_6]^{2-}$:

$TiO_2 + 6HF \rightarrow [TiF_6]^{2-} + 2H_2O + 2H^+$

(6)

In summary, the dissolution of titanium in solutions containing only HF occurs through reactions (1) and (2), in presence of $HNO_3$ via reactions (1) (5) and (6). Moreover, in addition to its oxidizing action, $HNO_3$ reacts with $H_2$:

$3H_2 + 2HNO_3 \rightarrow 4H_2O + 2NO$ (7)

In this way the risks related to hydrogen embrittlement are minimized. The alloy employed in this study is an $\alpha+\beta$ titanium alloy whose microstructure is reported in figure 8.

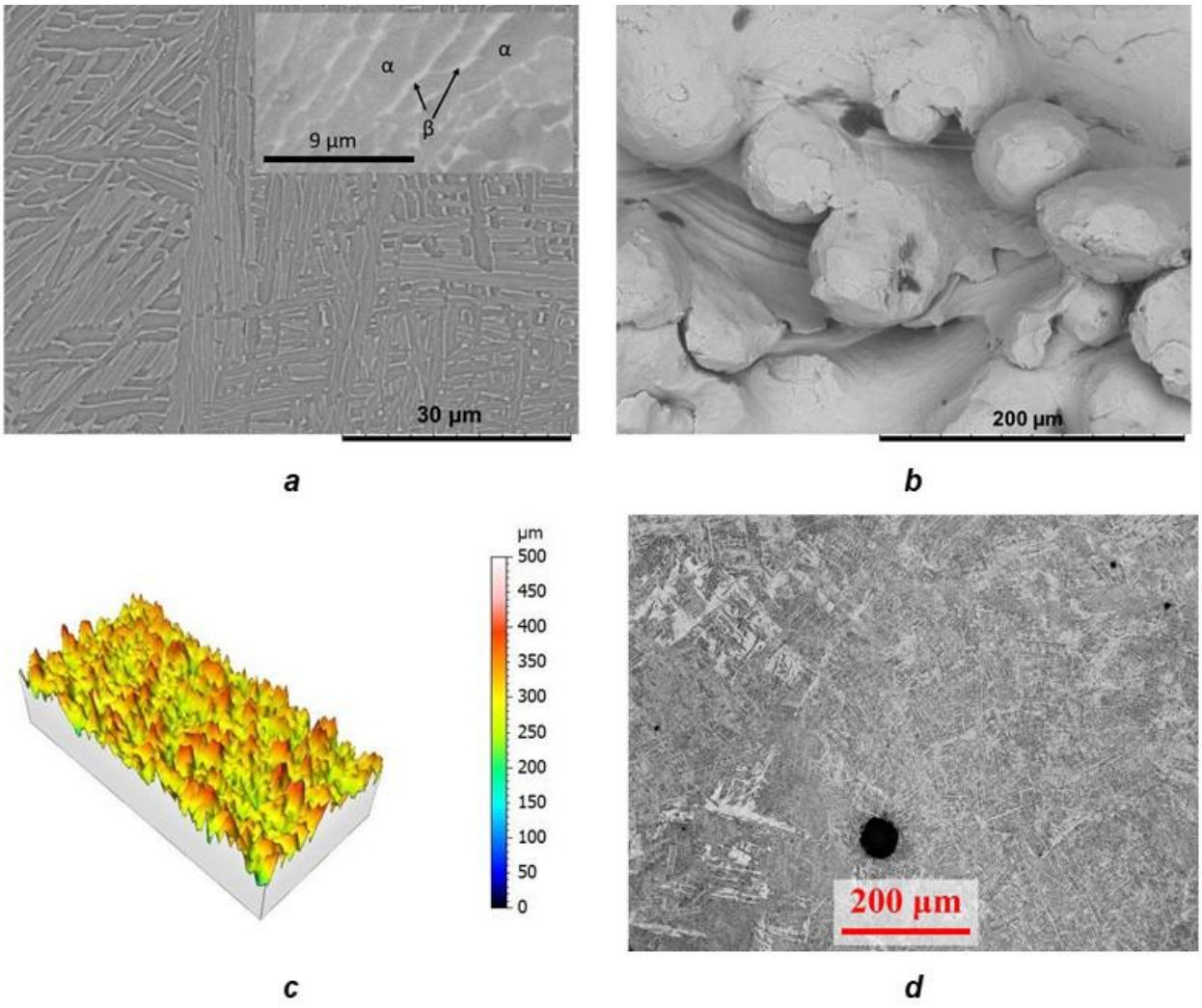


*Figure 8: (a) microstructure of EBM Ti6Al4V; (b) morphology of as received surface; (c) 3D reconstruction of as received surface; (d) cross section of an EBM specimen with round-shaped porosity.*

The microstructure is typical of α+β alloys that experience a high cooling rate from a temperature above the β-transus and it is made of thin α lamellae phase separated by lamellar β phase; the alloying elements, i.e. Al and V, are non-equally distributed among the two phases, Al is preferentially dissolved in the α phase and V in the β one [46]. In Figures 8b and 8c, the surface morphology of as built samples is reported. The surface is characterized by the presence of non-fused particles and other irregularities like pores and cracks. Moreover, the 3D reconstruction shows the presence of deep valleys and sharp edges. The values of surface parameters in as received condition are Sa = 37.5 µm, Sz = 448.8 µm, Pdq = 69.2°. A cross-section of the samples (figure 8d) shows the presence of internal porosity, the round-shaped pores being produced during the EBM process due to the development of gases [10].

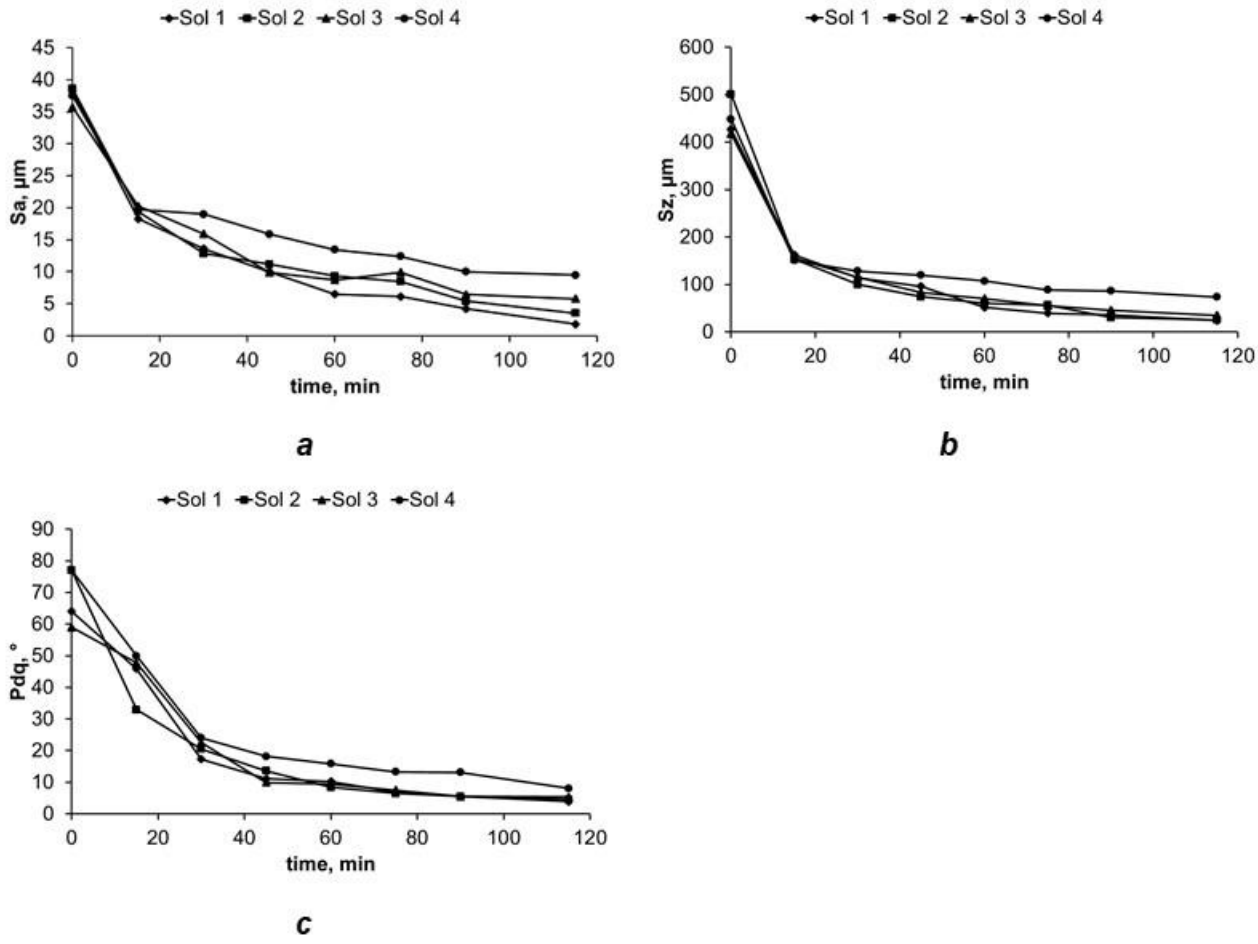


*Figure 9: trend of the different surface parameters during the process; (a) Sa; (b) Sz; (c) Pdq.*

In Figure 9a the trend of Sa as a function of immersion time is reported. It can be observed that Sa decreases for all the employed solutions. Moreover, the decreasing rate is higher during the first 15 min of treatment and then becomes lower.

A similar trend is observed for Sz and Pdq. In particular, the decrease of Sz indicates that the process is selective toward peaks, whereas the final values of Pdq demonstrate that the process has effective smoothing capabilities. The fast decrease of the parameters during the initial stage of the process is explained by the presence of non-fused particles. The chemical reactions reported above are surface reactions and the rate of the smoothing process is higher as it is higher the surface contact between metal and solution. The non-fused particles have a high specific surface and are selectively removed during the first part of the treatment.

After the removal of particles, the surface parameters continue to decrease, and during this stage, the smoothing of the surface is obtained by the mechanism described below.

The metal surface is made of alternating peaks and valleys. The reaction rate between metal and solution depends strongly on the transport of matter between the surface and the bulk of the solution, considering that inside the valleys the transport of matter is more difficult since the reaction product accumulates and the concentration of active acids decreases, meaning that the reaction rate is lower in the valley to respect peaks that are selectively removed [47].

The kinetic mechanism described above is based on the motion of ions from the surface to the bulk of the solution and vice versa. This motion is driven by a gradient of concentration and by an electric field, but according to the Faraday laws, the amount of electric charge produced in anodic areas is equal to the charge consumed in cathodic areas, meaning that the global electric field on the metal surface is null, and the transport of ions depends only by the gradient of concentration.

In this kinetic mechanism, the viscosity of the solution plays a key role. The diffusivity of ions decreases as the viscosity increases, and globally the reaction rate is lower, but the effect of viscosity is enhanced inside deep and shallow valleys due to their small section and the selectivity of the process toward peaks increases [46].

From Figure 9 and Table 3, it can be observed that the values of the different parameters at the end of the treatment are lower in solution with a higher concentration of HNO3.

In Table 4 viscosity of the different solutions estimated from the data available for the binary systems $H_2O$-$HNO_3$ and $H_2O$-HF is reported. The solution with the highest viscosity is solution 1 followed by solutions 2, 3 and 4. Highly concentrated HNO3 solutions have higher viscosity therefore a lower transport property and a higher smoothing capability.

| | Sa (µm) | Sz (µm) | Pdq (°) |
|---|---|---|---|
| **As Received** | 37.5 | 448.8 | 69.2 |
| **Solution 1** | 1.8 | 24.1 | 3.9 |
| **Solution 2** | 3.5 | 25.6 | 4.5 |
| **Solution 3** | 5.8 | 35.3 | 5.3 |
| **Solution 4** | 9.5 | 73.6 | 8.1 |

*Table 3: surface parameters of as received surface and after 2 hours of treatment in the different solutions.*

| | Solution 1 | Solution 2 | Solution 3 | Solution 4 |
|---|---|---|---|---|
| **Viscosity, Pa·s** | $1.6 \cdot 10^{-3}$ | $1.3 \cdot 10^{-3}$ | $1.2 \cdot 10^{-3}$ | $8.8 \cdot 10^{-4}$ |

*Table 4: estimated viscosity of the different solutions.*

In Figure 10, the topography of the metal surface after 2 hours of treatment in solutions 1, 2, 3 and 4 is shown. All the employed solutions make the surface smoother to the as-received case, but in the case of solutions 2, 3 and 4 the typical morphology with alternating peaks and valleys is still observable. Furthermore, for all the analyzed solutions the different surface parameters tend to have an asymptotic value, since as the surface becomes smoother and the valleys less deep and sharp, the selective mechanism of dissolution of peaks becomes less effective. For solution 4, the absence of $HNO_3$ leads to the development of gaseous $H_2$ on the metal surface, the gas bubbles acting as a barrier and the contact between solution and surface is bad, therefore the final quality of the surface is worse when compared to the ones obtained from the other solutions.

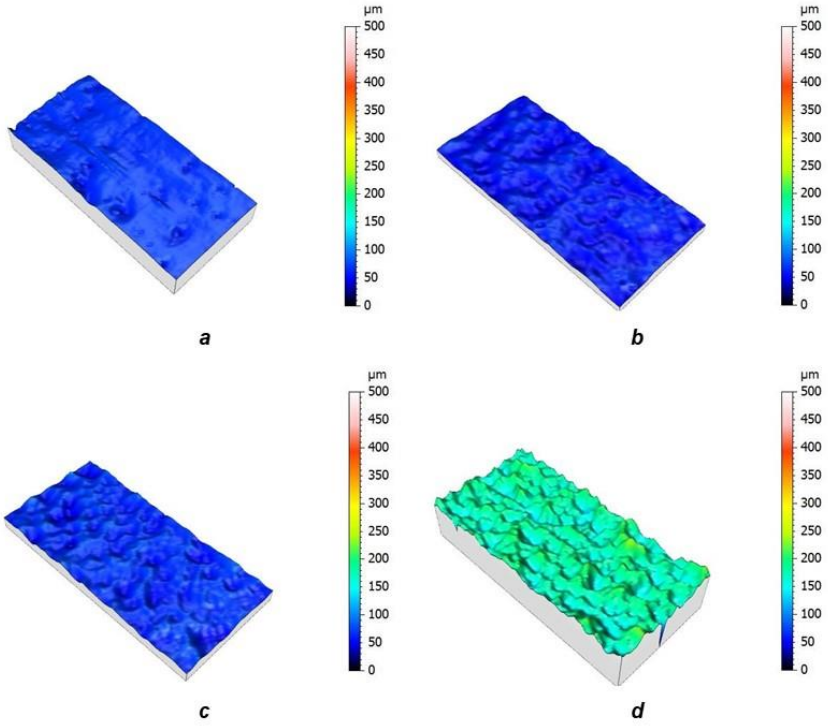


*Figure 10: surface topography of metal surface after 2 hours of treatment in (a) solution 1; (b) solution 2; (c) solution 3; (d) solution 4.*

Figure 11 shows the morphology of the surface after 2 hours of immersion in solution 1 and 4. For the received surfaces, the non-fused particles have been completely removed and the surface is definitively smooth with a homogeneous profile without deep valleys and sharp peaks, however, the internal porosity is still present.

At higher magnification factors the morphology of the treated surface is characterized by the presence of thin lamellae placed in relief to respect the base matrix. Comparing this

morphology with the microstructure of the alloy shown in Figure 8, it is evident that the thin lamellae are the β phase and the base matrix the α phase.

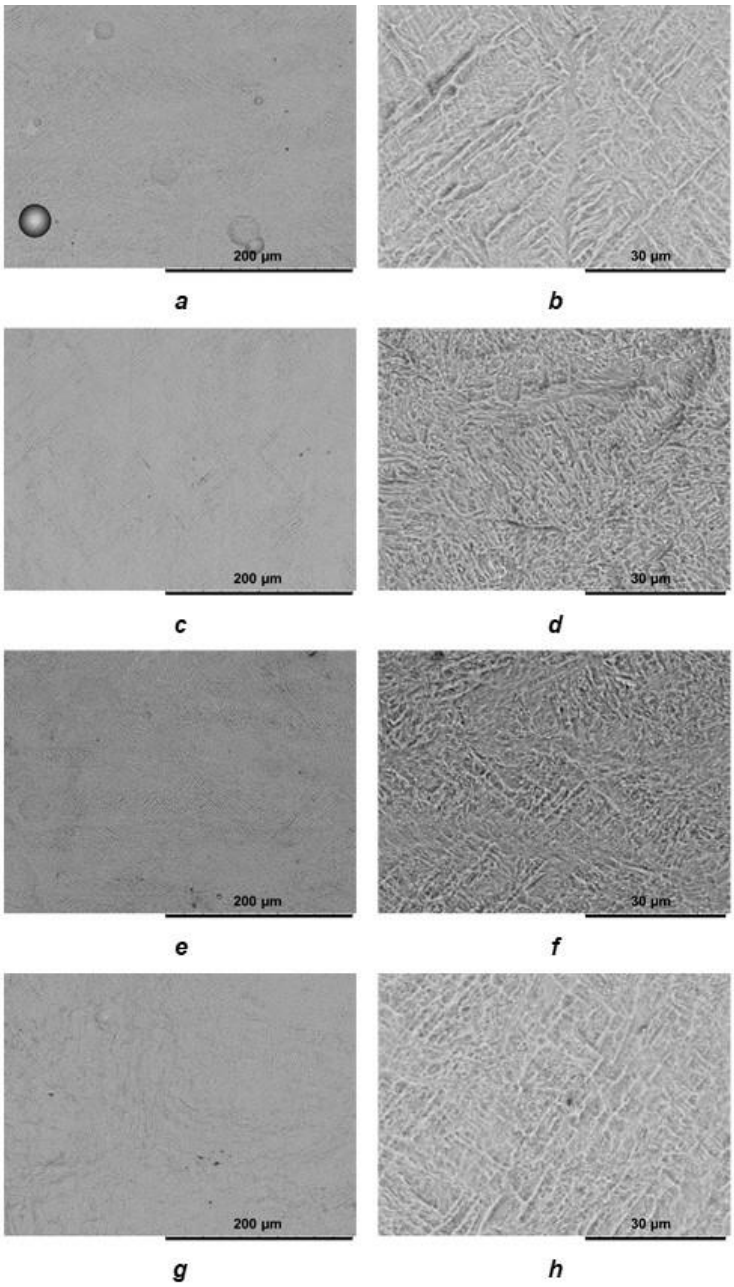


*Figure 11:* ***(a)*** *500X SEM micrography of metal surface after 2 hours of immersion in solution 1;* ***(b)*** *2500X SEM micrography of metal surface after 2 hours of immersion in solution 1;* ***(c)*** *500X SEM micrography of metal surface after 2 hours of immersion in solution 2;* ***(d)*** *2500X SEM micrography of metal surface after 2 hours of immersion in solution 2;* ***(e)*** *500X SEM micrography of metal surface after 2 hours of immersion in solution 3;* ***(f)*** *2500X SEM micrography of metal surface after 2 hours of immersion in solution 3;* ***(g)*** *500X SEM micrography of metal surface after 2 hours of immersion in solution 4;* ***(h)*** *2500X SEM micrography of metal surface after 2 hours of immersion in solution 4.*

As reported by Sefer et al [46], the treatment of Ti6Al4V with solutions containing HF and $HNO_3$ is selective towards the α phase that is preferentially dissolved with respect to the β phase. As said before, the nature of the reactions of Ti6Al4V with HF and HNO3 is

electrochemical and the dissolutions occur in the anodic areas. In the present case, the β phase behaves preferentially as a cathode and the α phase preferentially as anode, therefore the dissolution rate is higher on the α phase. This difference in electrochemical behavior between the two phases of the alloy is explained in terms of their composition, the high concentration of Al inside the α phase making it less noble if compared to the β one.

| | Ti (wt%) | Al (wt%) | V (wt%) |
|---|---|---|---|
| As Received | 90.09 | 6.45 | 3.46 |
| Solution 1 | 90.51 | 5.81 | 3.68 |
| Solution 2 | 91.02 | 5.29 | 3.69 |
| Solution 3 | 91.02 | 5.19 | 3.67 |
| Solution 4 | 91.86 | 4.24 | 3.94 |

*Table 5: surface composition of the metal surface after 2 hours of treatment in the different solutions.*

The measured composition of the surface after the dissolution process is reported in Table 5. For all the solutions an impoverishment of Al is noticed. This result is in agreement with the observed preferential dissolution of the α phase that in Ti6Al4V alloy solubilizes mainly the Al.

The impoverishment of Al on the surface is more evident after treatment in solution 4 which does not contain HNO3. In solution 4, the dissolution of the alloy occurs without the formation of an oxide layer. The passivating effect of $HNO_3$ leads to the formation of a $TiO_2$ layer, however, inside the oxide the other constituents of the alloy i.e. V and Al are also present. As reported by different authors the composition of the oxide is not the same as the base alloy and the different ligands redistribute on the surface during the passivation stage [47,48]. The true composition of passive oxide is a matter of debate and depends on many factors, but the results of the present work indicate that the passivation leads to a surface composition that minimizes the effect of the selective dissolution of the α phase and the consequent impoverishment of Al. This change in surface concentration can cause a change in the corrosion behavior of the metal, however, the surface treatments of titanium alloys with solution containing HF and HNO3 are common practice in biomedical applications where corrosion resistance is a major requirement [49].

In Figure 12 the averaged value of ER is reported for the different solutions. Solution 4 has the lower ER because, due to H2 development, the true exposed surface during the process

is lower when compared to the solutions containing HNO3. In the other cases, the ER increases with the concentration of HNO3. This result is explained by the fact that the increase in the acidity of the solutions leads to a higher dissolution rate of the passive film [50].

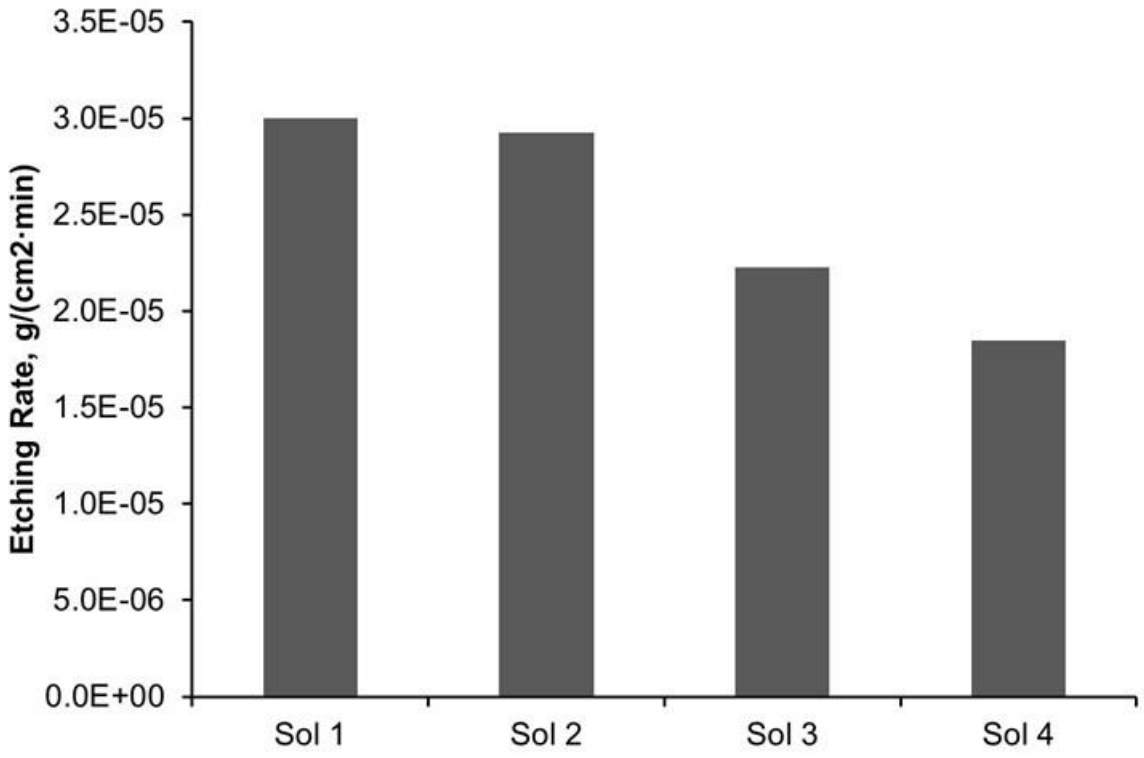


*Figure 12: Average values of ER for the different employed solutions.*

## Cylindrical geometry case

The effect of fluid velocity on the capability of chemical machining to reduce the surface roughness of EBM samples was studied in detail, to this aim cylindrical shaped samples with an initial diameter of 8 mm were immersed in the acidic solution and put in rotation around their axe for 90 minutes.

Three different conditions were analyzed: high rotational speed (HRS) corresponding to 450 RPM, low rotational speed (LRS) corresponding to 50 RPM, and finally stagnant (ST). An HF-HNO3 aqueous solution (HF (48 wt%) 39 ml, HNO3 (69 wt%) 225 ml, H2O 736 ml) was employed.

Every 15 minutes, the diameter reduction was measured, and surface topology was acquired in a covered area of 3X10 $mm^2$.

The three different treatments are effective in reducing surface roughness as demonstrated by Figure 13, in the best case analyzed the value of Ra decreased from the initial value of 7.69±0.59 µm to the final value of 0.82±0.03 µm.

The reduction of roughness by chemical machining occurs mainly because reaction products accumulate within the valleys where the reaction rate is lower if compared to peaks [46].

The roughness reduction occurred mainly in the first 15 min, as evidenced in the previous chapter, then the roughness decreased slowly toward an asymptotic value as shown in Figure 14, in fact at the beginning of the treatment the surface is characterized by deep and sharp valleys, and the effect of accumulation of reaction products is maximized, then, as the surface becomes smoother the treatment efficiency decreases.

The final chemically machined surface is characterized by a predominant waviness and the final value of Sa depends mainly on Wa, to this scope the chemical solution is not effective in reducing Wa because waviness surface is made of round and smooth profiles and, as said before, the chemical solution is effective forward sharp profiles.

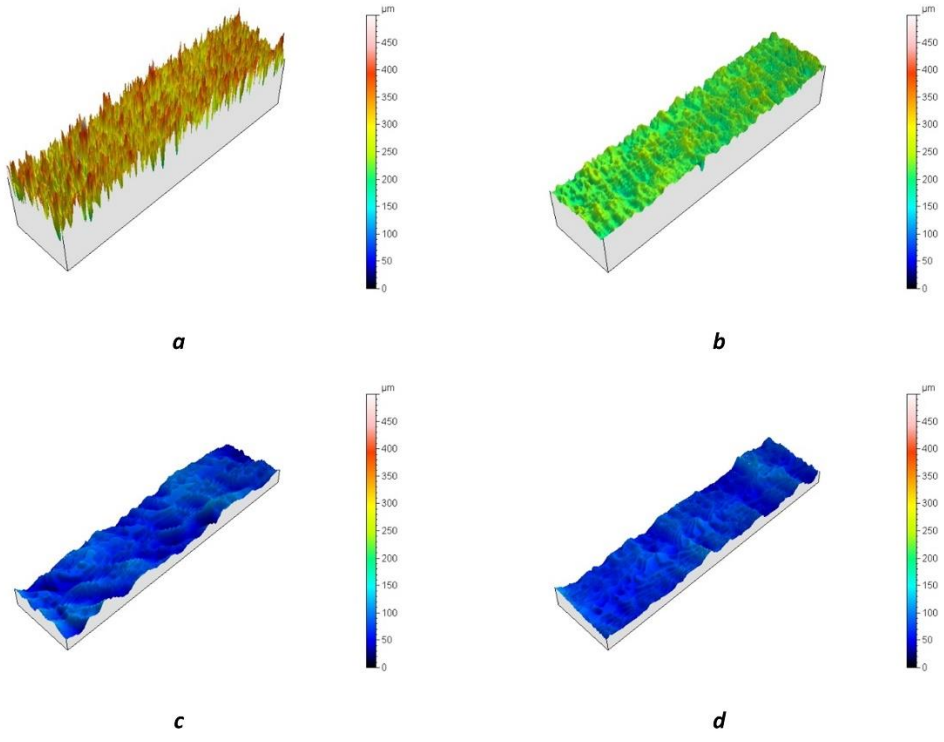


*Figure 13: (a) Surface morphology and Sa in as built condition, (b) after ST treatment, (c) after LRS treatment and (d) HRS.*

The presence of waviness also in the case of stagnant condition excludes that it is due to some fluid dynamic cause, however, the origin of waviness is unclear and, probably, it is

related to the pre-existing layer-by-layer structure of the EBM samples. At the end of the chemical treatment the measured roughness of HRS results lower even if comparable to LRS, in both these conditions the final Ra is smaller than the stagnant case, instead in terms of Wa no differences are noticed between the three treatments. On the contrary, the treatments differ in terms of diameter reduction, as shown in Figure 14c, the HRS condition results in the highest etching rate followed by LRS and ST

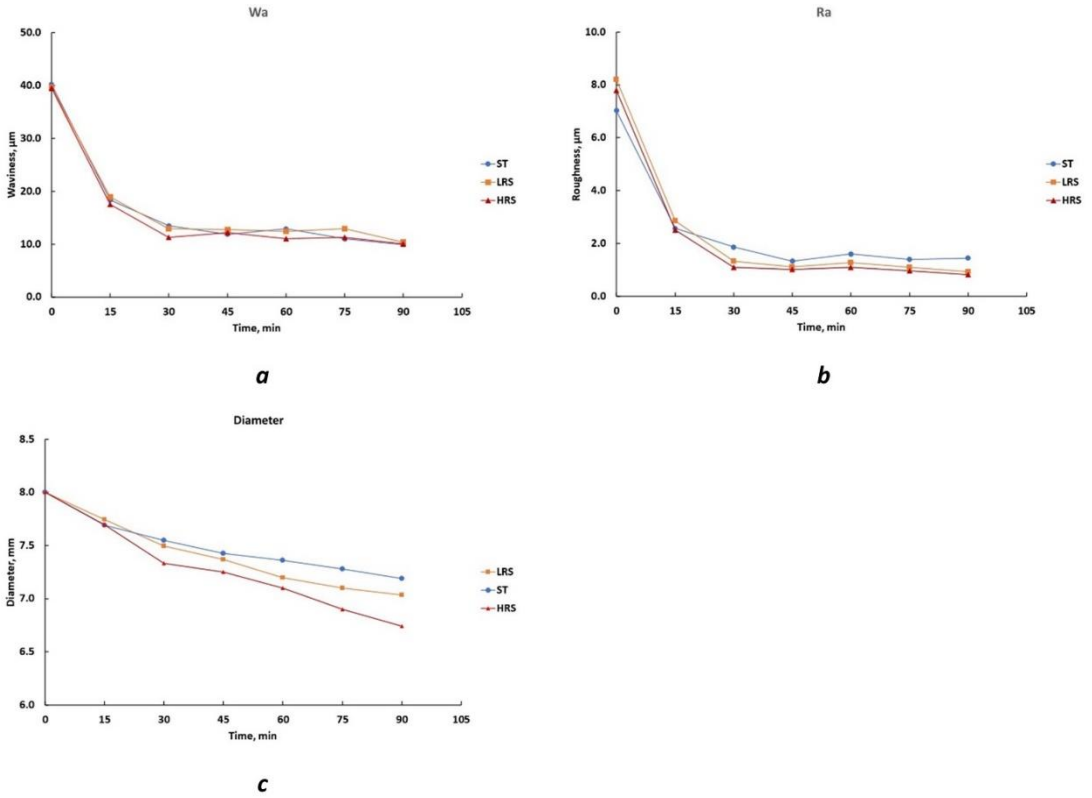


*Figure 14: Trend of (a) Wa, (b) Ra and (c) diameter in ST, LRS and HRS conditions.*

The three employed conditions correspond to different fluid dynamics regimes, the evaluated Reynolds numbers for as-built specimen:

$$Re = \frac{\Omega r^2}{\eta}$$

where Ω (rad/s) is the angular velocity, r (m) is the cylinder radius, and η (m2/s) is the kinematic viscosity equal to 1.4·10-6 m2/s in the present case, are reported in table 6.

| | ***ST*** | ***LRS*** | ***HRS*** |
|---|---|---|---|
| ***Re*** | 0 | $1.1 \cdot 10^4$ | $1.0 \cdot 10^5$ |

*Table 6: Evaluated Reynolds numbers for the three different conditions.*

Obviously, Re=0 in stagnant condition while LRS correspond to moderate turbulence and HRS to strong turbulence.

In the case of stagnant flow, the mass transfer between the metal surface and solution occurs via molecular diffusion and the concentration gradient on the surface is the driving force of the process, in turbulent regimes the diffusion sublayer, i.e., the zone across which mass transfer occurs, depends on Re and it decreases as Re increases. In smooth surfaces, the entire mass transfer between solid and solution is driven by molecular diffusion inside the diffusion sublayer.

Furthermore, if the surface is smooth the diffusion sublayer is well developed and the only effect of increasing Re is to lower the sublayer thickness, in this way, the concentration drop between the surface and bulk solution occurs at a smaller distance with the consequence that the concentration gradient increases and so mass transfer (see figure 15a).

Different is the case of rough surfaces, if the roughness is much smaller than the diffusion sublayer thickness, the diffusion sublayer is not perturbated by fluid motion and the mass transfer occurs in the same way as smooth surfaces. However, if the roughness is comparable to the diffusion sublayer the effect of fluid motion is to break the sublayer; small eddies are generated on the surface and the mass transport mechanism is no more molecular diffusion but convection inside the eddies zone with the effect of increasing mass transfer rate (see figure 15b).

In a rough surface made of alternating peaks and valley, the effect of enhanced mass transfer does not concern the fluid inside the valleys where the eddies difficulty penetrates and the fluid is stagnant, but the action of the eddies is strong around the peaks where the dissolution rate is very high.

In the present case the thickness of the diffusion sublayer was estimated to be comparable to Sa in both LRS and HRS conditions [48, 49] The turbulence is responsible for the higher values of etching rate and the lower value of final roughness. Moreover, the increase of turbulence level increases the kinetic energy of eddies and their mass transport capability.

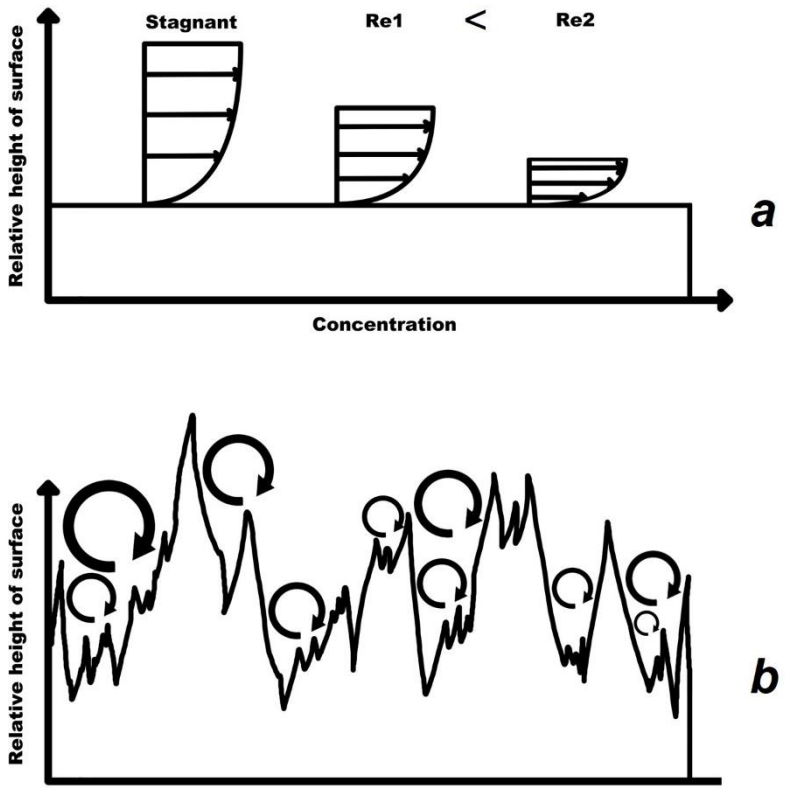


*Figure 15: (a) effect of Reynolds number on diffusion sublayer thickness on smooth surfaces; (b) formation of turbulent eddies on rough surfaces.*

## Fatigue validation

The possibility of 3D printing titanium alloys creates new opportunities for designing and manufacturing load-carrying components [34], but fatigue behavior needs to be further investigated [36, 37]. Most studies [38, 39] are based on the investigation of the build direction influence on fatigue performance, some researchers focus attention on the influence of beneficial heat treatments to reduce the dimensions of internal defects [40, 41]. Regarding surface modification treatments [34], researchers in literature have extensively investigated the impact of machining while there's a considerable gap of knowledge on the fatigue behavior of additively manufactured parts after tool-less treatments, especially chemical finishing. For these tests, specimens were treated in HRS condition since this condition resulted in the lowest value of Ra.

The as-built AM Ti6Al4V fatigue behavior is well studied in the literature, and it is well known that surface finishing of parts has an impact on fatigue life, particularly the life under high cycle fatigue (HCF) conditions [50].

To evaluate the influence of chemical finishing in terms of fatigue life, a preliminary study on a few samples for axial fatigue testing [51] has been conducted and it has been integrated later with a bigger test campaign of rotating beam fatigue testing on Ti6Al4V EBM samples.

Axial fatigue testing has been carried out using an Amsler HFP 250 axial fatigue testing machine on treated specimens and, when failure occurred, fracture surfaces were analyzed using a HITACHI TM3000 scanning electron microscope. Fatigue tests were carried out for two stress levels (378 MPa and 310 MPa), frequency of the tests was set to 71 Hz with a fatigue stress ratio of 0.1. Samples geometry was defined according to the ASTM E466 standard, as shown in Figure 16.

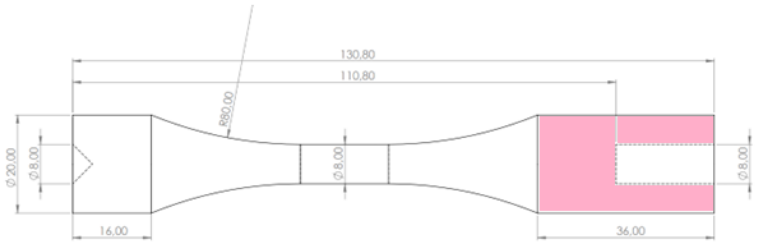


*Figure 16: Specimen geometry according to ASTM E466 standard. The red area is a sacrificial part conceived to ease the chemical treatment.*

The solution was capable of reducing Sa after 1 hour and 30 minutes of treatment as shown in figure 17.

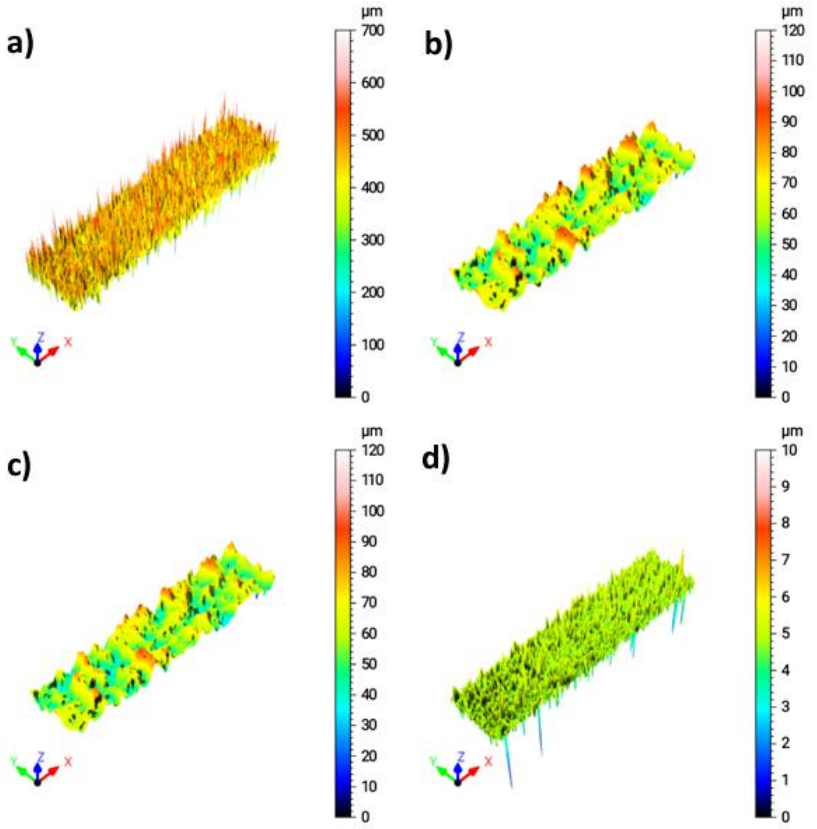


*Figure 17 Base surface before (a), after treatment (b); waviness (c) and roughness (d) of treated surface.*

Acquisitions highlight the treatment effectiveness: Sa decreased from an average value of 35.92 µm to 9.05 µm, while the diameter of the specimen was reduced from an average value of 19.92 mm to 18,54 mm. Finally, a comparison between the waviness and roughness of treated and untreated surfaces evidences the fact that the solution is capable of reducing Ra (<1 µm) but can't reduce Wa below certain values (~9 µm). Table 7 summarizes the effect of chemical treatment.

| | Untreated (µm) | Treated (µm) |
|---|---|---|
| S | 35.92 | 9.05 |
| W | --- | 8.91 |
| R | --- | 0.78 |

*Table 7: Surface quality before and after chemical treatment*

The measurements demonstrate that as built surface is mainly rough with a linear base profile characterized by a random alternation of peaks and valleys from a median plane in

the case of as-built specimens. Treated specimen surfaces have been analyzed separating waviness and roughness, using a Gauss filter with a cut-off of 0.08 mm, the surface results are mainly wavy with a very low roughness. The treatment is effective in reducing roughness and the final Sa is mainly dependent on waviness. Such evidence can be related to the fact that solution is intrinsically selective for surface peaks rather than for the valleys, where reaction products tend to accumulate.

The five treated specimens have been fatigue tested at two different stress levels. Two specimens have been subjected to 378 MPa and three to 310 MPa. Specimens subjected to 378 MPa failed around $10^5$ cycles while two out of three specimens subjected to 310 MPa stress didn't fail and reached runout. However, the third specimen subjected to 310 MPa failed prematurely, due to critical defects enhancing cracks initiation. A resume of the fatigue tests is reported in table 8.

| Specimen | Smax (MPa) | Mean Load (kN) | Amplitude (kN) | Frequency (Hz) |
|---|---|---|---|---|
| **ST-1** | 378 | 8,07 | 6,83 | 71 |
| **ST-2** | 310 | 6,56 | 5,59 | 71,4 |
| **ST-3** | 310 | 6,12 | 5,23 | 71 |
| **ST-4** | 310 | | | 70,6 |
| **ST-5** | 378 | 8,07 | 6,83 | 70,5 |

*Table 8: Fatigue testing results*

Fracture surfaces have been analyzed through Scanning Electron Microscope to highlight the surface contribution in terms of fatigue crack initiation. For each specimen (ST1, ST5 and ST2) the crack initiation site has been detected and acquired. Some internal defects are brought to the surface due to the material removal. ST1 specimen cracking is initiated by a pore brought to the surface while ST5 failure occurs because of cracking initiation starting from a subsurface pore, as can be evidenced by Figure 18 respectively finally ST2 specimen premature failure, instead, is caused by a lack of fusion.

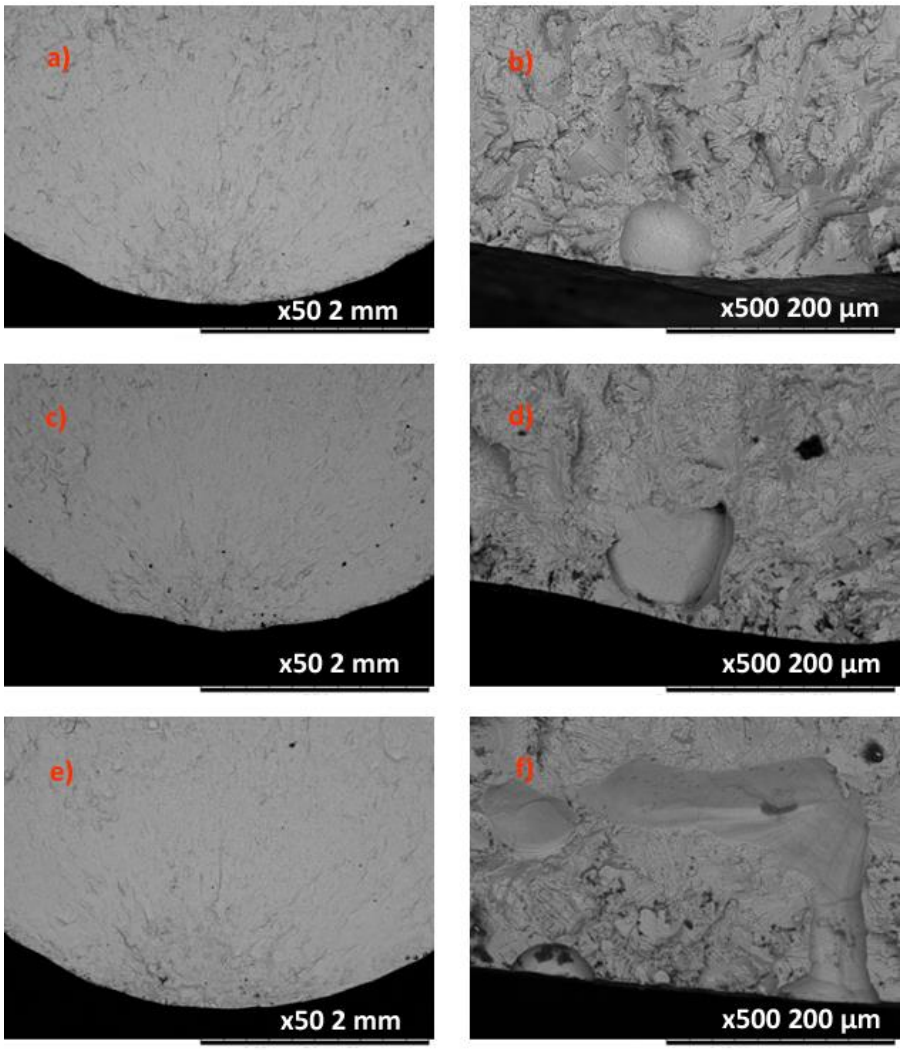


*Figure 18: ST1 specimen panoramic view (a) and detail on the crack initiation site (b) (superficial pore);*

The fatigue limit obtained by this preliminary study proves that surface treatment is effective in enhancing fatigue behavior if compared to the as-built specimen results (100-200 MPa) [50, 52]. On the other hand, the measurements obtained are more dispersed because failures are related to the random defect distribution in the bulk material. In the case of EBM untreated specimens, crack initiation occurs mainly on the surface, to this aim the employed chemical treatments mitigate the detrimental effects of poor surface quality. In Figure 19, the results from this campaign are resumed and compared with the data from the literature, highlighting the similarities between the case of chemically treated samples and the turned samples, compared with as-built samples performance.

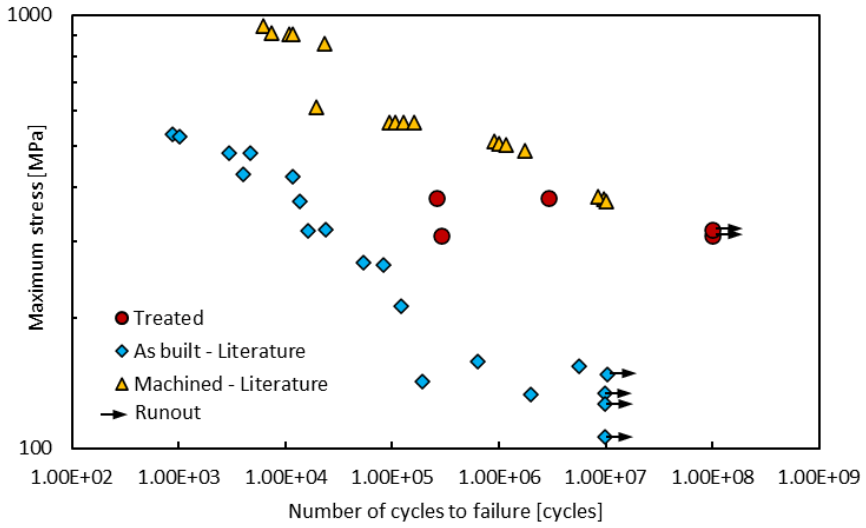


*Figure 19: Fatigue behavior of as built and machined specimens from the literature [14], compared to the chemical machined specimen.*

With these encouraging results, an experimental campaign on rotating beam fatigue testing has been carried out.

The tests have been performed using an experimental rotating beam fatigue testing setup, designed, and produced in collaboration with a local company. Constant amplitude rotating beam fatigue testing was performed with a stress ratio of R = -1 while load frequency was set to 70 Hz at room temperature [51]. Three different stress levels have been investigated: the maximum stress tested was 900 MPa to determine the LCF fatigue limit (around the $10^3$ cycles life); 300 MPa was set to highlight the fatigue limit (considering $10^7$ cycles as runout) according to preliminary results from the above-mentioned work and literature findings [53–55] for AM Ti6Al4V fatigue tests, and a middle-stress level was imposed at 500 MPa to provide further information to the experimental curve. The as-built and treated specimens fatigue curves were obtained by testing three specimens for each stress level, finally HITACHI TM3000 scanning electron microscope and Nikon SMZ 745T stereomicroscope were used to examine the fracture surfaces after failure. The geometry of rotating beam fatigue testing samples was defined according to the ISO1143 standard, as shown in Figure 20.

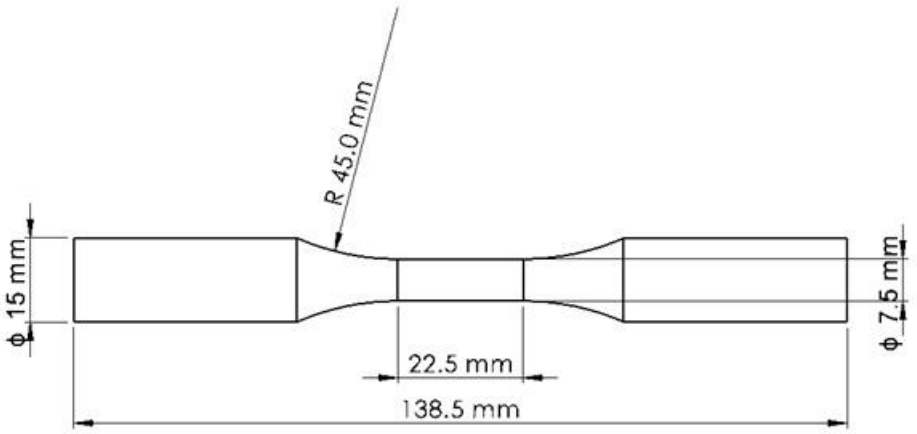


*Figure 20: Detailed geometry of fatigue specimen.*

Rotating beam fatigue testing has been carried out on both as built specimens and chemically machined specimens in HRS condition since this condition resulted in the lowest value of Ra. The chemical treatment results in an enhancement of fatigue behavior, particularly on HCF life, in fact, at the stress level of 300 MPa all the as built specimens undergo failure while two treated samples experienced runout and the third failed at about $2 \cdot 10^6$ cycles as shown in figure 21.

Fracture surfaces were analyzed to highlight their main features and treatment influence. Depending on the stress level and starting surface quality, it is possible to highlight the differences between treated and untreated fracture surfaces after fatigue testing.

The chemical treatment results in an enhancement of fatigue behavior, particularly on HCF life, in fact, at the stress level of 300 MPa all the as built specimens undergo failure while two treated samples experienced runout and the third failed at about $2 \cdot 10^6$ cycles as shown in figure 21.

Fracture surfaces were analyzed to highlight their main features and treatment influence. Depending on the stress level and starting surface quality, it is possible to highlight the differences between treated and untreated fracture surfaces after fatigue testing.

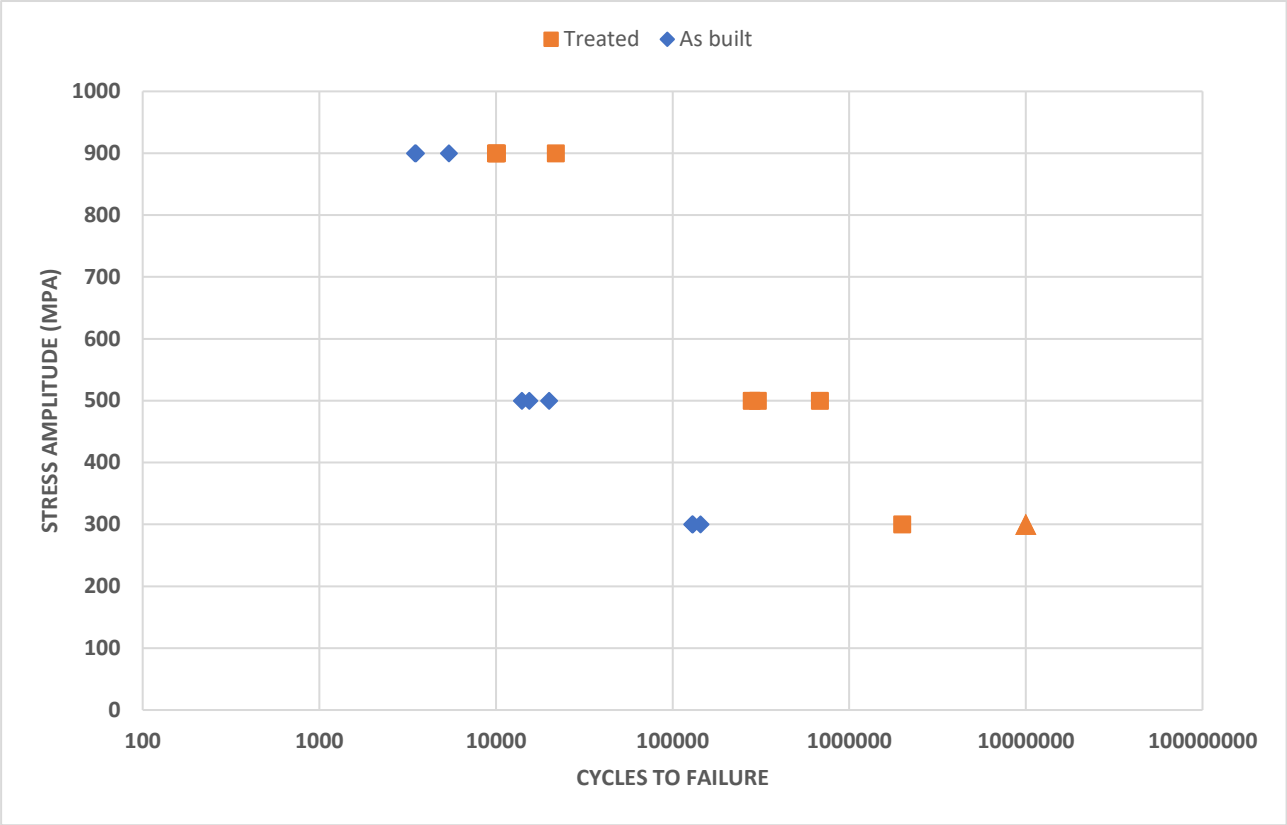


*Figure 21: Whoeler's curves for treated and as built Ti6Al4V EBM fatigue specimens.*

Specimens subjected to the maximum stress (900 MPa) exhibit different fracture surfaces, particularly the as built case has multiple crack initiation sites evidenced by a circular shiny zone on the outer part of the surface, the multiple crack initiation observed is compatible with the profile reported in figure 22b; the treated part, instead has different shiny areas originated by single defects, superficial or sub-superficial, brought to surface by the chemical treatment. In this case, the fracture surface is more like a mild stress concentration case.

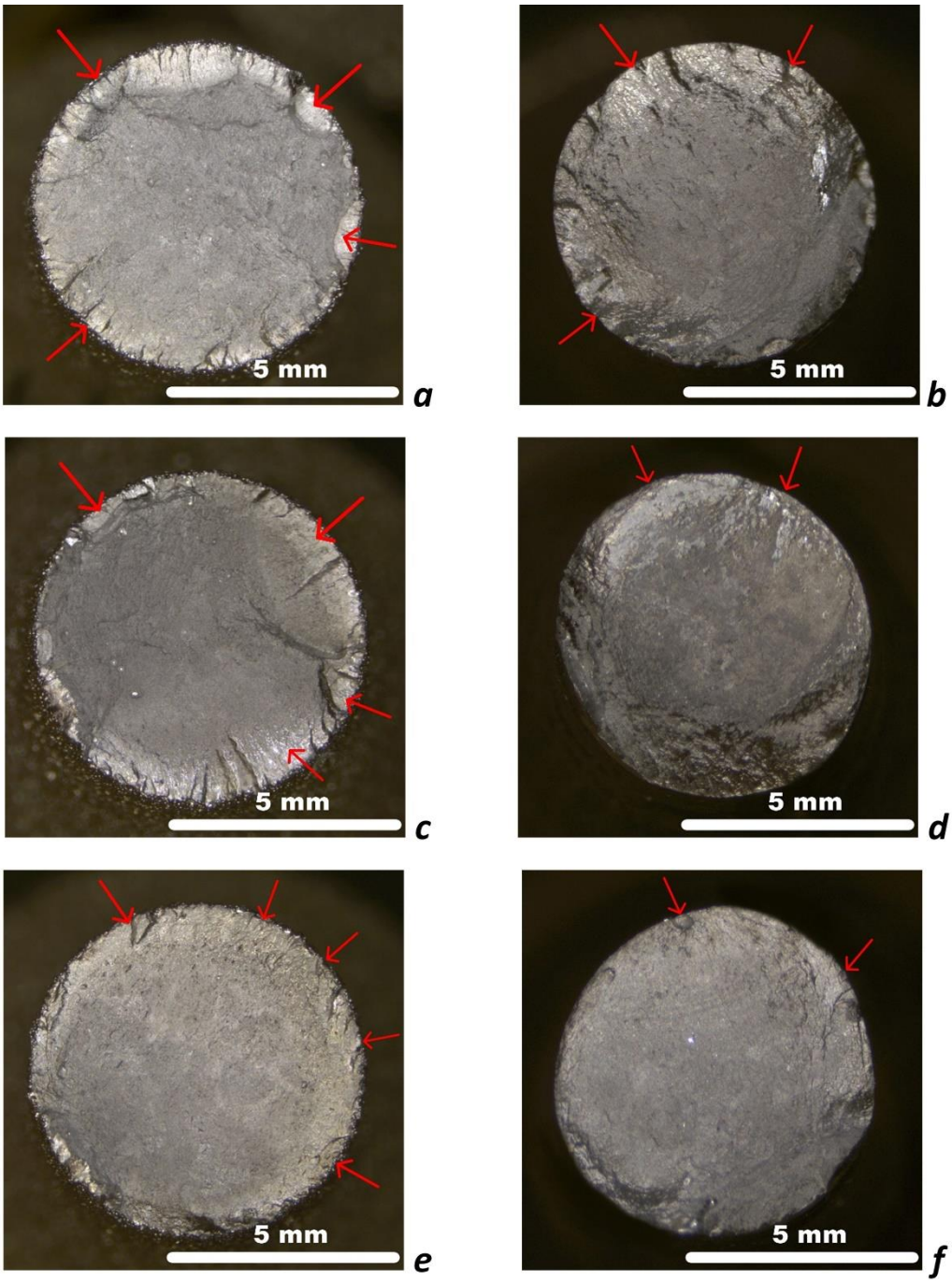


*Figure 22: Comparison between as built and treated specimen fracture surface, at different stress levels: a) as built specimen stressed at 900 MPa; b) treated specimen stressed at 900 MPa; c) as built specimen stressed at 500 MPa; d) treated specimen stressed at*

The stress of 500 MPa results in a similar surface morphology to the case of 900 MPa with a small difference in the dimensions of crack propagation and failure areas. Also, in this case, the untreated specimen is characterized by a shiny circular zone while the treated specimen has evident tracks of crack propagation originating from metallurgical defects.
Finally, the 300 MPa stress level was enough for detecting failure in untreated specimens while a fatigue limit was found for treated specimens. However, one of the three treated parts failed prematurely because of a big pore brought to the surface from the treatment, the pore is evident in both pictures 22d and 23b.
An SEM inspection is capable of further detailing the different cracking initiation systems, as shown in figure 23. Image (a) shows the multi-cracking system typical of the untreated specimens while image (b) highlights the cracking initiation from single defects. Images (c) and (d) respectively represent the crack propagation and fracture zone which are similar on both treated and untreated specimens. The propagation area is characterized by the typical morphology deriving from R = -1 fatigue stress type, exhibiting compression bands deriving from the alternate stress. The fracture zone, instead, is characterized by dimples typical of a ductile failure.

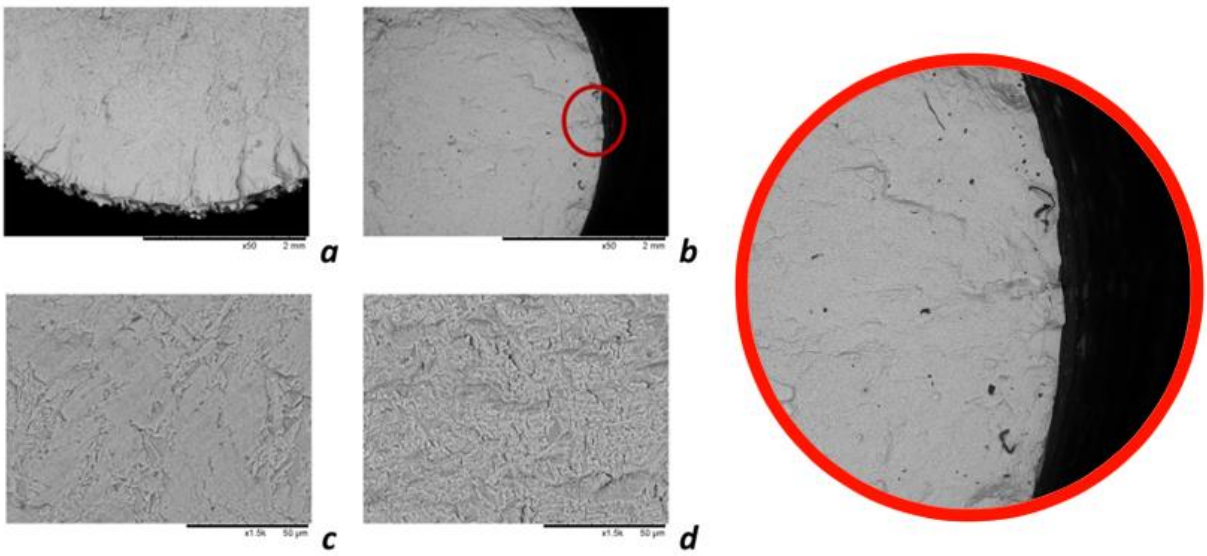


*Figure 23: SEM acquisitions: (a) crack initiation on the surface for the untreated specimen; (b) crack initiation site from metallurgical defect near surface for the treated specimen; (c) crack propagation zone; (d) fracture zone.*

To sum up, for untreated specimens, cracking initiates from multiple superficial sites, while for treated parts cracking always initiates from a specific site (generally a superficial/sub-superficial flaw).

## Laser polishing

In this section, the effectiveness of laser polishing in improving the surface quality of Ti6Al4V axisymmetric parts produced using two additive manufacturing techniques, namely Electron Beam-Powder Bed Fusion (E-PBF) and Laser-Powder Bed Fusion (L-PBF), is analyzed and compared. To this aim, the Design of Experiments (DoE) approach was used to investigate the effects of laser polishing on the surface quality of the parts. Moreover, microstructure analysis through optical microscopy and SEM was carried out to check the evolution of the processed surface. Within the designed and investigated laser polishing windows, the results showed that laser polishing produced an appreciable surface quality improvement of both L-PBF and E-PBF Ti6Al4V cylinders of 52% and 68% respectively. Other important outcomes are related to the notable differences in the initial roughness of the L-PBF and E-PBF parts, affecting the performance of laser polishing: E-PBF parts had a rougher profile (around 50 µm) if compared to L-PBF parts (around 10 µm), which required a different approach for the polishing of the two categories of samples. Despite power levels being the same, to process EBM multiple passes were necessary which led to the use of higher rotational speeds in order to reduce the laser residence time and avoid overmelting.

Figure 24 shows the SEM images of the respective powders used for the fabrication, whose chemical composition is also reported in Table 1. The size range was the following: from 20 to 60 µm for the L-PBF process; and from 45 and 106 µm for the E-PBF process.

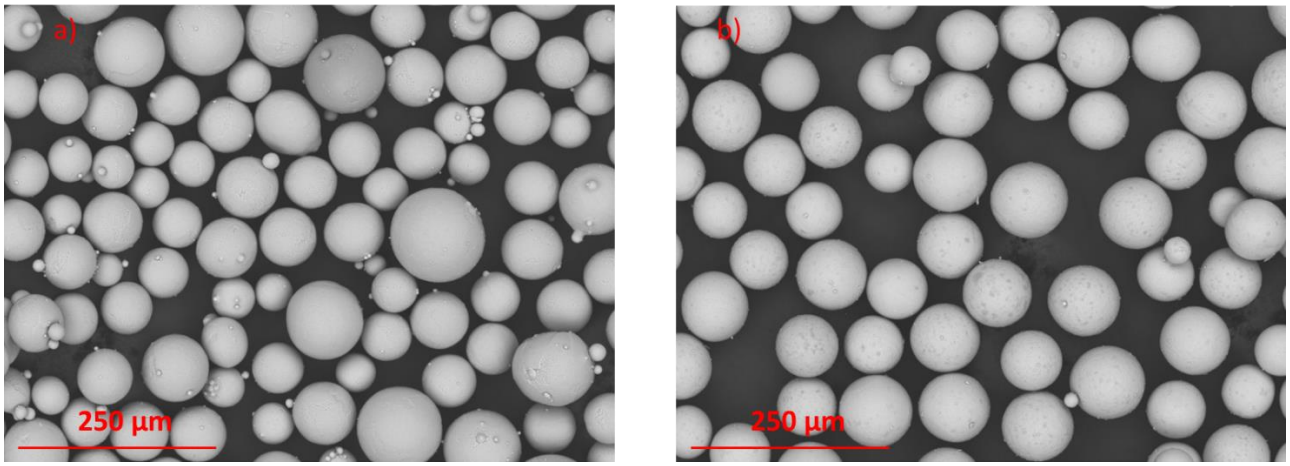


*Figure 24: SEM images of the powder feedstocks used for: a) E-PBF and b) L-PBF.*

The L-PBF specimens were produced employing a Renishaw AM250 machine, with the following process parameters: laser power = 350 W, hatch distance = 55 µm, layer thickness = 30 µm. The printing process was carried out in Argon atmosphere. The build platform was preheated to 730 °C to minimize distortion and for better control over cooling rates, and the scanning strategy was raster type with a rotation of 67° between two consecutive layers.

For the E-PBF specimens, an Arcam A2X E-PBF machine was used. The specimens were produced according to the following parameters: gun voltage = 60 kV, hatch distance = 55 µm, layer thickness = 90 µm. It's important to note that this process requires a high vacuum level, with an interlock on the chamber pressure demanding $1.6\times10^{-4}$ mBar before starting the high voltage supply. The electron beam unit necessitates $8.0\times 10^{-7}$ mBar or lower to ensure the cathode lifetime. The build platform was maintained at a temperature of 730 °C, and the beam scanning, carried out according to the integrated speed function supplied by Arcam for the selected alloy, was raster-like similar to the L-PBF process.

| | Element | Ti | Al | V | Fe | O | Residual | C | N | H |
|---|---|---|---|---|---|---|---|---|---|---|
| Renishaw AM250 | wt% | Balance | 5.5 to 6.5 | 3.5 to 4.5 | <0.25 | <0.13 | <0.1 (single) <0.4 (total) | <0.08 | <0.03 | <0.0125 |
| Arcam A2X | | Balance | 5.5 to 6.8 | 3.5 to 4.5 | <0.30 | <0.20 | <0.1 (single) >0.4 (total) | <0.10 | <0.05 | <0.015 |

*Table 9: Chemical composition of the powder feedstocks.*

## Laser polishing for EBM and SLM cylindrical samples

The geometry of the specimens used for polishing, according to the Figure 25 sketch, was the same for both E-PBF and L-PBF processes, with a 7.5 mm diameter and a length of 50 mm.

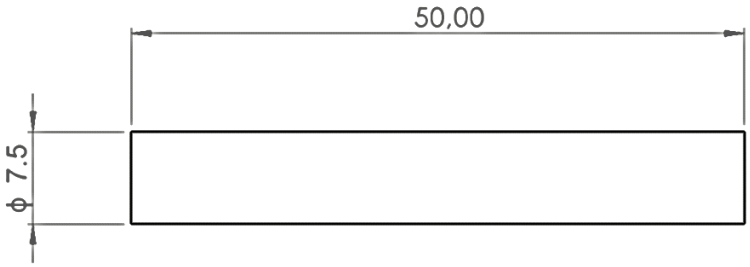


*Figure 25: Sketch of the typical specimen used for laser polishing optimization on cylindrical parts.*

The laser polishing process was performed using a ROFIN DC-15 1.5 kW $CO_2$ laser, with the technical specifications listed in Table 10. The test samples were connected to the variable speed DC motor using a holding chuck to facilitate the rotational movement., as shown in Fig. 26a. This assembly was mounted onto the positioning stage of the $CO_2$ laser, as shown in Fig. 26b. The CNC control system was utilized to control the translational movement of the stage, enabling linear displacement of the sample with reference to the fixed laser beam as shown in Fig. 3a. By combining both linear and rotational motions, a series of overlapping laser scanning tracks (OV) were generated, effectively covering the targeted surface area during the scanning process [25].

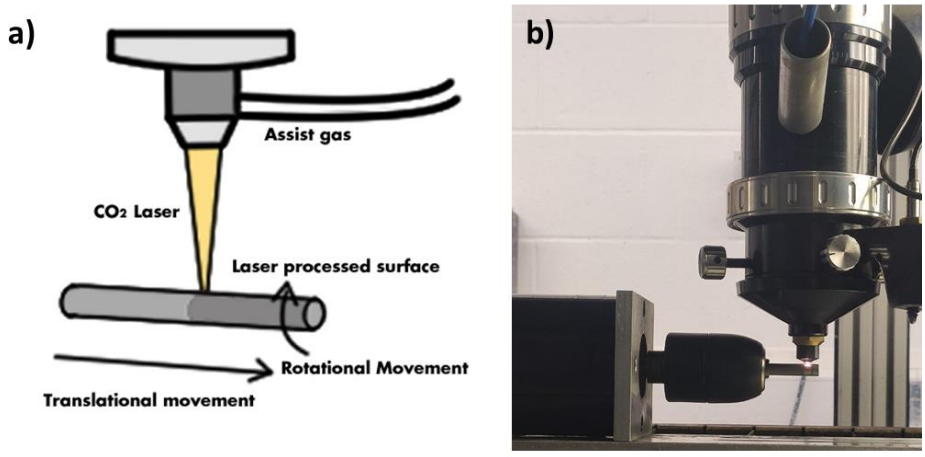


*Figure 26: a) Sketch of the laser polishing setup; b) Actual experimental setup.*

| | |
|---|---|
| Max power | 1500 W |
| Beam wavelength | 10.64 µm |
| Beam quality factor $M^2$ | 1.05 |
| Laser focus diameter | 0.2 mm |
| Max. scanning speed | 5000 mm/min |
| Max. rotational speed | 5000 rpm |
| Assist gas | Argon |
| Work mode | CW |

*Table 10: Technical specifications of ROFIN 1.5 kW CO2 laser.*

Following an approach based on a previous study conducted by Obeidi et al. [25] and after performing several preliminary tests, the influence of the most significant processing parameters was investigated based on a Design of Experiment DoE model.: More specifically, a Box-Benkhen design (BBD) with three factors in three levels considered. The factors taken into account were the laser power, the percentage overlap between the laser

tracks and number of passes. The chosen polishing parameters used for E-PBF and L-PBF specimens respectively are reported in Tables 11-12. Consequently, considering five repetitions of the centerpoint, a total of 17 polishing experiments were carried out for each specimen type, as reported in Tables 13 and 14. All the laser polishing experiments were carried out with a laser spot of 200 µm and using Argon shielding gas at a pressure of 0.3 bar. The controlling parameters chosen for the BBD were overlap, laser power and number of passes. Overlap can either be controlled by varying linear speed or rotational speed, for L-PBF parameters from previous work were taken into account [25], controlling the overlap tracks was carried out by varying the rotational speed. The results from the L-PBF BBD were meant to be used as a starting point for the E-PBF BBD. After some preliminary tests, using the best parameters combination from the L-PBF BBD on E-PBF samples, it was noted that the parameters weren't affecting the surface significatively, as expected, since the topology samples surface is completely different: the L-PBF were characterized by low Sa if compared to the E-PBF ones and this affects the laser polishing process. For this reason, more passes (2 to 4, rather than 1 to 3) were required to treat E-PBF samples but, to avoid over melting, rotational speed was required to be higher than the L-PBF case thus it was set as a controlling parameter for overlap.

| **E-PBF** | Power (W) | OV (%) | Number of Passes | Translational speed (mm/min) | Rotational speed (RPM) |
|---|---|---|---|---|---|
| Level 1 | 135 | 0 | 2 | 60 | 300 |
| Level 2 | 150 | 33 | 3 | | 450 |
| Level 3 | 165 | 55 | 4 | | 600 |

*Table 11: Factors and levels considered for the BBD of laser polishing of E-PBF specimens.*

| **L-PBF** | Power (W) | OV (%) | Number of Passes | Traslational speed (mm/min) | Rotational speed (RPM) |
|---|---|---|---|---|---|
| Level 1 | 135 | 0 | 1 | 20 | 200 |
| Level 2 | 150 | 25 | 2 | 30 | |
| Level 3 | 165 | 55 | 3 | 40 | |

*Table 12: Factors and levels considered for the BBD of laser polishing of L-PBF specimens.*

The surfaces of both the as-built and laser-polished samples were characterized by using the Bruker Contour GT confocal microscope. The instrument was equipped with the VISION 64® software for data analysis, surface profile visualization, and surface roughness description term evaluation. For the surface acquisitions, a 1x1.2 mm area was investigated.

Concerning the measured outputs, it was decided to analyze the mean areal surface roughness, Sa, and maximum peak-to-valley distance, Sz, defined according to the ISO25178 standard. Moreover, given the adoption of a DoE approach for the experiments, it was decided to analyze the effects of the treatment and its input variables on the surface quality through the Response Surface Method (RSM). In this way, assuming a 95% confidence interval (i.e. $\alpha = 0.05$), the correlation between the input and output variables was analyzed also from a statistical point of view through a multivariate ANOVA.
Afterward, the surface morphology inspection before and after the laser polishing was analyzed through a Zeiss EVO LS-15 SEM, whereas microstructural and chemical composition analysis was carried out, after a metallographic preparation of the specimens, through optical microscopy (Zeiss Axioskop 40) and SEM-EDS (Hitachi TM3000 SEM – Oxford Instruments SWIFTED3000 EDS probe). For the microstructure analysis, the metallographic specimens were etched with the Keller's reagent by swabbing for 20 s.

### Laser surface polishing of E-PBF specimens

For the case of the E-PBF specimens, it was found that the mean surface roughness (Sa) of the untreated specimens was 54.3 ± 4.1 μm, presenting therefore a very rough surface. This result was expected considering the nature of the E-PBF process, involving powders with larger size in the first place in comparison with L-PBF as well as a more intense thermal interaction due to the electron beam in substitution of the laser [56]. For what concerns the effects of laser polishing, Fig. 27 shows the response surfaces related to Sa as the output, sorted by the laser power levels. As visible from the 3D plots, the effects of the investigated process variables fall within a linear correlation model, given the appreciable but not steep differences in Sa among the BBD combinations. In general, the main experimental outcome was that the laser polishing had a significant effect on the surface quality of E-PBF specimens, with an average final value of about 17.3 ± 3.3 μm, indicating therefore an average Sa reduction of 68% over the starting values. This appreciable reduction of roughness can be seen also from the SEM image reported in Fig. 28 which shows that the huge amount of sintered powders on the surface due to the E-PBF process were completely removed after polishing but, at the same time, leaving a wavy mark on the underlying surface morphology.

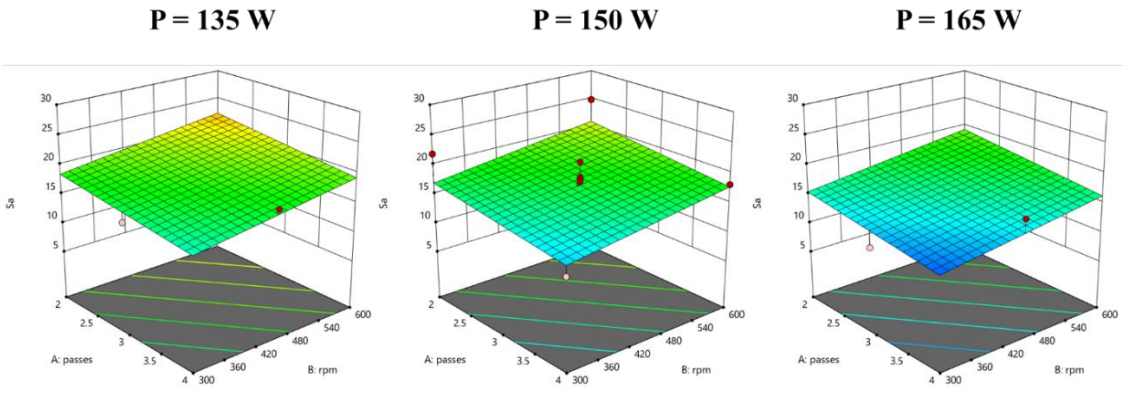


*Figure 27: Response surfaces obtained for the E-PBF specimens after laser polishing. The plots show the correlation between Sa and passes-rpm, for each level of laser power. The red points indicate experimental values greater than the predicted, and vice versa for the white ones.*

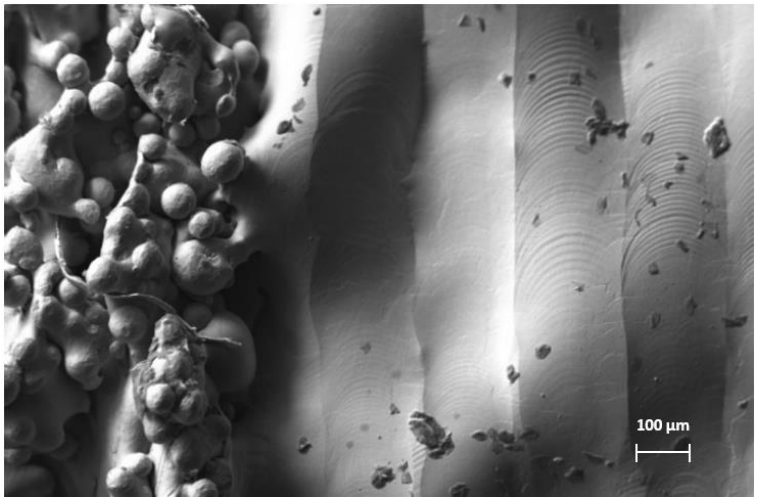


*Figure 28: SEM image taken at the interface between the as-E-PBF and laser-polished surfaces, showing the significant improvement of the surface quality. The picture shows the best results obtained from the Box Benkhen of E-PBF.*

However, despite the appreciable improvement of the surface quality, the investigated processing window did not allow for the exploitation of significant correlations between the inputs and Sa. More specifically, despite the requirements of normality and randomness of the variance being satisfied, as visible in Fig. 29, the ANOVA results showed that the levels chosen for the factors were not providing statistical significance, as noticeable from the ANOVA summary data reported in Table 13. In other terms, the influence of the operating parameters on the surface modification entity was not sufficiently different among the processing combinations to draw robust conclusions. Indeed, the regression analysis led to a signal-to-noise ratio of 4.39, hence slightly sufficient to proceed with the regression according to the Design Expert software indications, and an adjusted R2 of 0.17, that suggests an overall weak correlation between the model terms, i.e. the input variables, and Sa. This outcome can be also seen according to the p-value results reported in Table 13, showing that in every case it was greater than the fixed confidence value of 0.05.

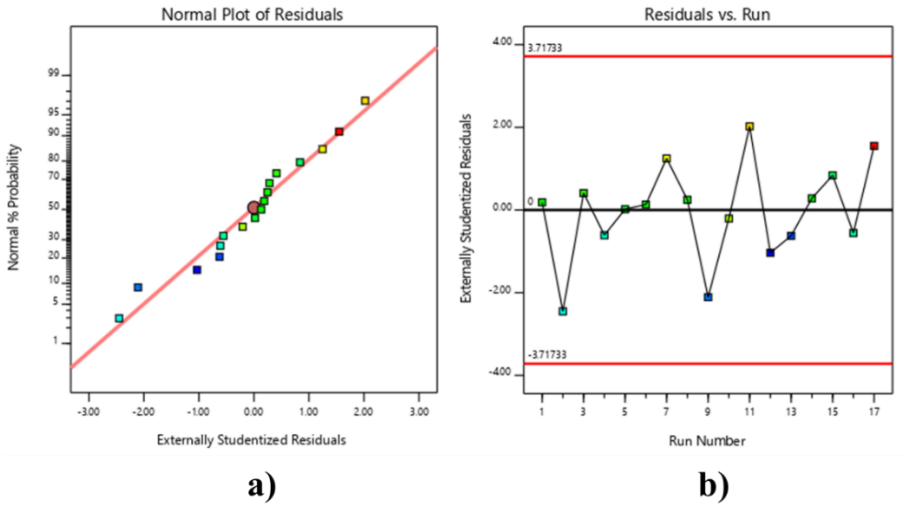


*Figure 29: a) Normal probability plot of the post-laser polishing residuals, showing that the results meet the requirement of data normality for the subsequent regression; b) Analysis of variance vs run number, showing the absence of specific trends that suggest the absence of systematic experimental errors.*

*Table 13: Model fitting summary for the laser polishing BBD of E-PBF specimens.*

| | Sum of Squares | Degrees of freedom | Mean Square | F-value | p-value |
|---|---|---|---|---|---|
| Model (linear) | 67.03 | 3 | 22.34 | 2.10 | 0.1493 |
| No. of passes (A) | 18.94 | 1 | 18.94 | 1.78 | 0.2047 |
| RPM (B) | 29.88 | 1 | 29.88 | 2.81 | 0.1174 |
| Laser power (C) | 18.21 | 1 | 18.21 | 1.71 | 0.2131 |

The poor statistical robustness of the model could be interpreted according to the analysis of the phenomena behind the observed experimental outcomes. The experimental results proved the feasibility of the laser polishing process in reducing the surface roughness of E-PBF specimens, however, Fig. 28 showed clearly that the greatest contribution of this reduction was due to the melting and ablation of the sintered powders, leaving a jagged and wavy surface. These latter residual texture characteristics could be ascribed to two main factors: i) the high initial surface roughness: as the laser's ability to re-melt the superficial material depends on the energy input in the first place, there is evidence in the literature that the laser polishing of rough surfaces such as the ones typical of powder-based AM could benefit of an enhanced absorption due to multiple rebounding of the beam into the asperities [57, 58]. On the other hand, when the initial surface roughness is very high such as in this case, this benefit could be limited and might lead to a relatively lower surface quality compared to the LPBF samples. Achieving high surface quality (low Sa and Sz values) is correlated to more exposure to the laser beam, more melting and may include some material

removal. This in turn means applying more thermal energy followed by unrequired chemical and microstructural changes so was avoided. Therefore, the presence of superficial bumps on the polished surface might be due to the residues of the original topography lying underneath the sintered powders layer; ii) the focal position of the laser on the specimen surface: in this work, the laser spot was set as equal to its focus, placed at the same height of the surface peaks. Consequently, taking again into account the irregularity and asperities height variation of the as-built surface, a small beam diameter with a close focal position could affect detrimentally the robustness of the re-melting mechanism against these height differences. Hence, the possibility of better discriminating the efficiency of different combinations of power, speed and OV% becomes more difficult, leading to the closeness of the results shown in Fig. 4. As a matter of fact, experimental evidence of the benefits of surface quality improvement deriving from the laser defocusing was already discussed elsewhere [58]. Further evidence that supports this point could be seen from the optical macrograph illustrated in Fig. 30, showing a cross-section of the interface as-built-polished surface, taken along the specimen axis. As the asperities observed in the as-built surface appear very high, it is convincible that the laser was not able to transfer energy for re-melting in a balanced way against the different peaks and valleys, introducing conversely also a waviness component on the polished surface due to the insufficient re-melting energy. Furthermore, Fig. 30 highlights, as expected, the presence of a re-molten superficial layer, whose depth was around 100 μm and their microstructure features were quite comparable to the ones of the parent alloy, as shown from the SEM-EDS results illustrated in Fig. 31 and Fig. 32 respectively.

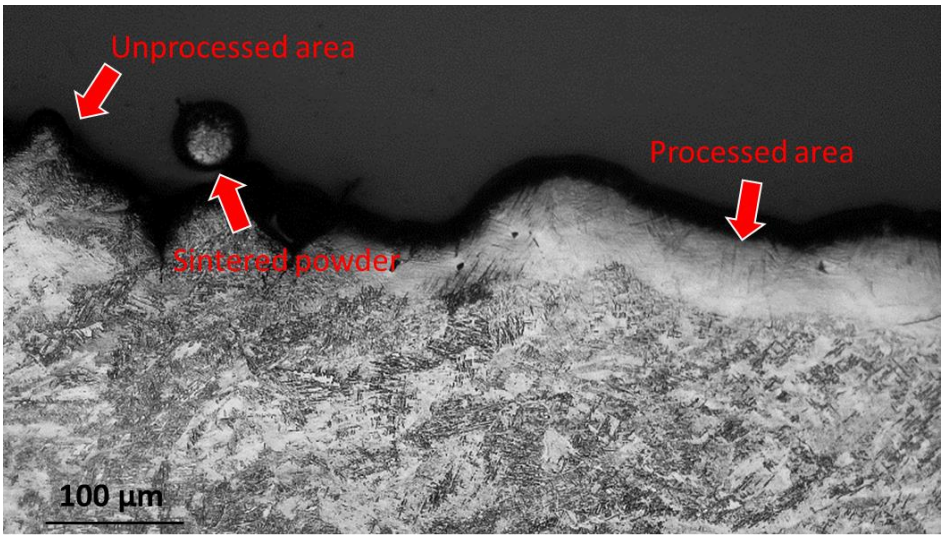


*Figure 30: Optical macrograph of a laser-polished E-PBF specimen, taken at the interface between the as-built and polished areas (magnification 100x)*

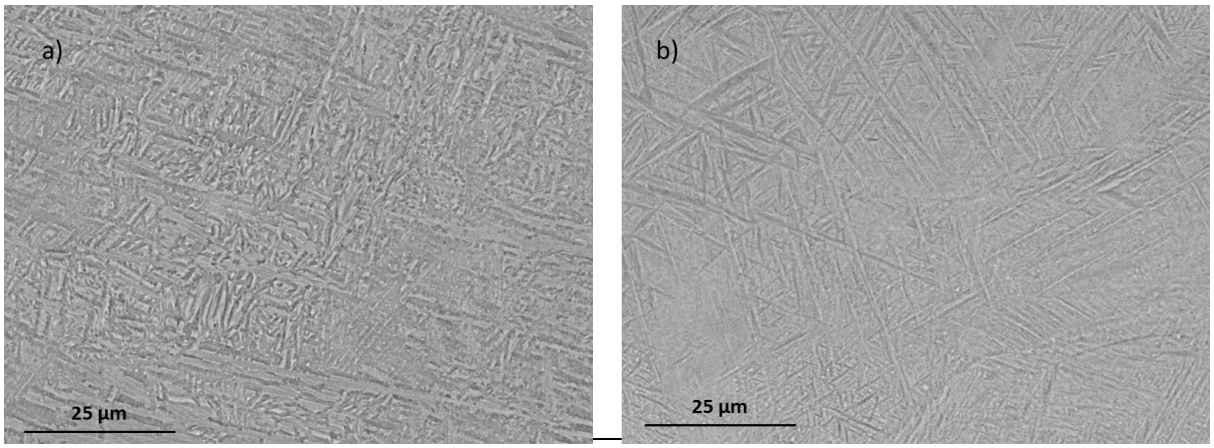


*Figure 31: SEM micrographs illustrating the microstructure of the: a) Base material; b) Re-molten zone (magnification 2000x).*

.

| Element (wt%) | Ti | Al | V |
|---|---|---|---|
| BM | 90.8±0.1 | 5.1 ±0.1 | 4.0 ± 0.1 |
| RZ | 90.2±0.1 | 5.8±0.1 | 4.0 ± 0.1 |

*Figure 32: Chemical composition data of the base material and re-molten zone, obtained through EDS analysis*

## Laser surface polishing of L-PBF specimens

For the case of the L-PBF specimens, it was found that the mean surface roughness (Sa) of the un-treated specimens was 10.2 ± 1.08 µm, showing therefore a smoother surface texture compared to E-PBF. However, despite this expected outcome, the response surfaces illustrated in Fig. 9 highlight that the influence of the polishing variables on Sa was more evident in comparison to the E-PBF case. More specifically, it can be noted that: i) the response surface indicated as optimal a number of passes of 2; ii) for the conditions related to a high-residence time of laser on the surface (low translation speed, high number of passes), an increase of the laser power had a negative effect on the polishing efficiency. Overall, the laser polishing produced a surface roughness reduction of the L-PBF specimens of about the 52%, with a final value of 5.35 ± 0.5 µm. Once again, the quantitative results were supported by the SEM inspection of the surface, indicating a remarkable surface modification occurred through the removal of sintered powder formed by balling. Moreover, it is also interesting to observe that the underlying morphology was flatter than the E-PBF typical one, giving therefore evidence that the different as-built surface has a great influence on the polishing efficiency.

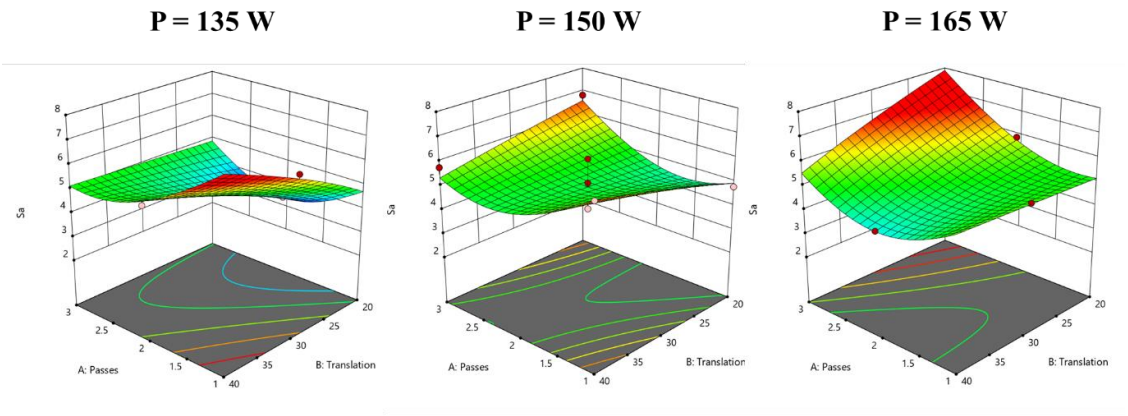


*Figure 33 Response surfaces obtained for the L-PBF specimens after laser polishing. The plots show the correlation between Sa and passes-translation speed, for each level of laser power. The red points indicate experimental values greater than the predicted, vice versa for the white ones.*

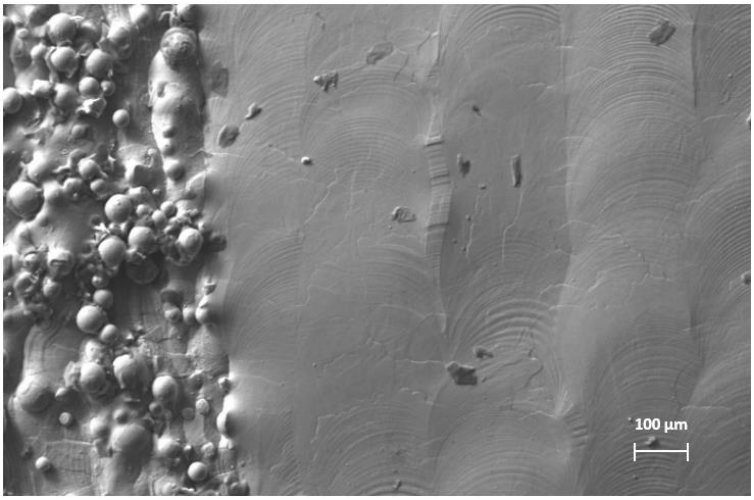


*Figure 34 SEM image taken at the interface between the as-L-PBF and laser polished surfaces, showing the significant improvement of the surface quality. The picture shows the best results obtained from the Box Benkhen of L-PBF.*

As visible from the curvature of the response surfaces reported in Fig. 33, a higher-order fitting model (quadratic) was found to be the best for the L-PBF polishing case. As for the E-PBF one, the check of the fitting residuals normality and randomness of the variance vs experiments ID was carried out through Design Expert ®, whose results are reported in Fig. 35. The results indicated again that the experimental data were suitable for the surface regression. Concerning the latter, Table 14 shows the fitting model summary and the terms chosen for the model. Besides the factors chosen for the polishing experiments, the model included also coupled interfering factors and a time-autocorrelation factor related to the number of passes. It is worth mentioning that the same quadratic terms for the translation speed and power were removed from the model, as they were constant for each experiment and therefore not meaningful for the regression. Overall, the regression analysis led to a

signal-to-noise ratio of 8.64 and an adjusted R2 of 0.7, suggesting therefore a stronger correlation between the input variables and Sa. However, according to the p-values reported in Table 14, it can be seen that the statistically significant terms were the interaction factors and the quadratic term for the number of passes. This result should be not surprising according to the following considerations: i) laser polishing relies on the heat input provided by the laser, whose way of adduction is regulated through the scanning factors (in this case, translational speed and the number of passes), it is convincible that the overall process dynamics is dictated by the combination of the provided energy input and the residence time of the laser over a defined area, hence providing more physical sense of grouped variables against the individual ones. However, the latter were still kept in the model as they were chosen as the actual inputs; ii) the re-melting ability of the laser depends strongly on the number of consecutive passes, either from a surface status and thermal history points of view. For the former aspect, even if the surface is smoothed after the first laser pass, the processed material is still able to absorb the radiation and experience re-melting, as also proven in critical cases like aluminum [59]. Furthermore, the benefits of the multiple consecutive passes could benefit from the heat build-up effect experienced by the specimen as it helps to stabilize the melting pool by reducing local temperature gradients.

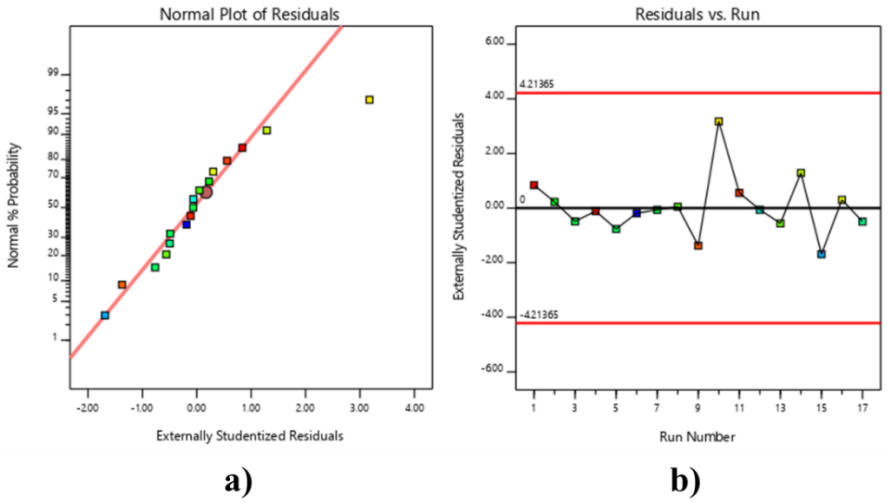


*Figure 35 a) Normal probability plot of the post-laser polishing residuals, showing that the results meet the requirement of data normality for the subsequent regression; b) Analysis of variance vs run number, showing the absence of specific trends that suggests the absence of systematic experimental errors.*

| | Sum of Squares | Degrees of freedom | Mean Square | F-value | p-value |
|---|---|---|---|---|---|
| Model (quadratic) | 1484.5 | 7 | 212.1 | 6.26 | 0.0069 |
| No. of passes (A) | 2.34 | 1 | 2.35 | 0.0691 | 0.7985 |
| Translation speed (B) | 17.12 | 1 | 17.12 | 0.5058 | 0.4950 |
| Laser power (C) | 33.34 | 1 | 33.34 | 0.9848 | 0.3469 |
| AB interaction | 302.75 | 1 | 302.75 | 8.94 | 0.0152 |
| AC interaction | 290.16 | 1 | 290.16 | 8.57 | 0.0168 |
| BC interaction | 291.39 | 1 | 291.39 | 8.61 | 0.167 |
| A time-autocorrelation ($A^2$) | 547.44 | 1 | 547.44 | 16.17 | 0.0030 |

*Table 14 Model fitting summary for the laser polishing BBD of L-PBF specimens.*

Concerning the influence of the as-built surface morphology of the specimens on the effectiveness of laser polishing, a variable to which particular attention was given in this work by selecting two AM processes, support to all the observed experimental and statistical outcomes can be found by looking the optical macrograph reported in Fig. 36. The macrograph shows that surface morphology of the as-L-PBF condition is more stable compared to the E-PBF case, in terms of the waviness underlying the sintered powders layer. Consequently, the laser re-melting sensitivity against the surface height differences is reduced, still valid the enhanced radiation absorption mechanism through the rough initial surface, especially for the first laser pass. In any case, it is still expected that an upward defocusing of the laser beam could contribute to a further improvement of polishing and increase the roughness reduction. For what concerns the microstructure evolution of the laser-processed surface, similar consideration of the E-PBF case can be drawn, as the re-molten layer depth was again around 100 μm, as visible in Fig. 36, and no significant microstructural nor chemical composition alterations occurred according to the results reported in Fig. 37 and Table 15 respectively.

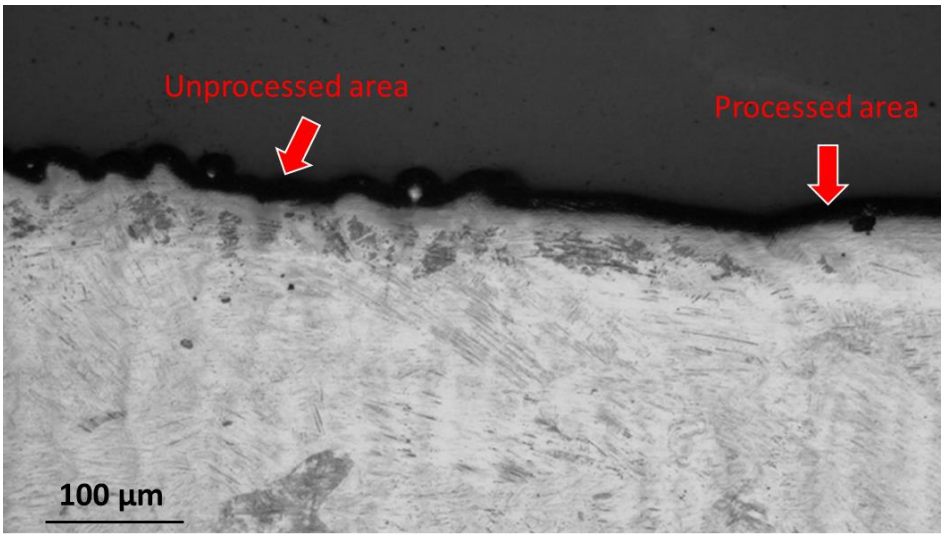


*Figure 36 Optical macrograph of a laser-polished L-PBF specimen, taken at the interface between the as-built and polished areas (magnification 100x)*

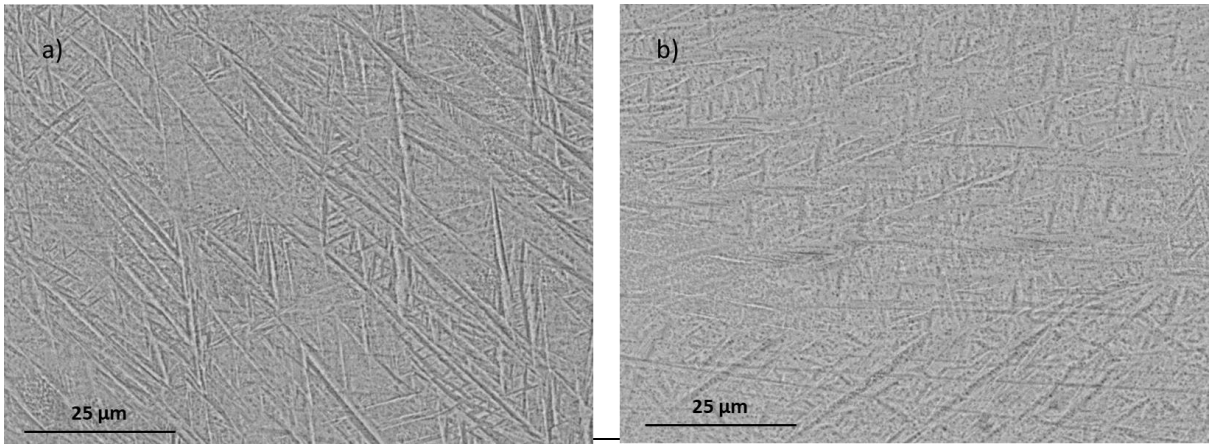


*Figure 37 SEM micrographs illustrating the microstructure of the: a) Base material; b) Re-molten zone (magnification 2000x).*

| Element (wt%) | Ti | Al | V |
|---|---|---|---|
| BM | 90.0±0.2 | 5.9 ±0.1 | 4.1 ± 0.2 |
| RZ | 90.3±0.2 | 6.0±0.1 | 3.7 ± 0.2 |

*Table 15 Chemical composition data of the base material and re-molten zone, obtained through EDS analysis.*

## Fatigue validation

Both SLM and EBM samples were manufactured according to ISO1143 standard, the same way as the EBM samples used for chemical machining (see fig. 20). A comparison between the as-built case and the treated case has been carried out using three stress levels (300 MPa, 500 MPa, 900 MPa) and 70 Hz as the frequency for the load application (same testing parameters as the EBM as built vs chemically machined case of the previous chapter).
The best parameters' combination determined from the previous Box Benkhen designs have been used to polish SLM and EBM samples respectively in order to minimize Sa.

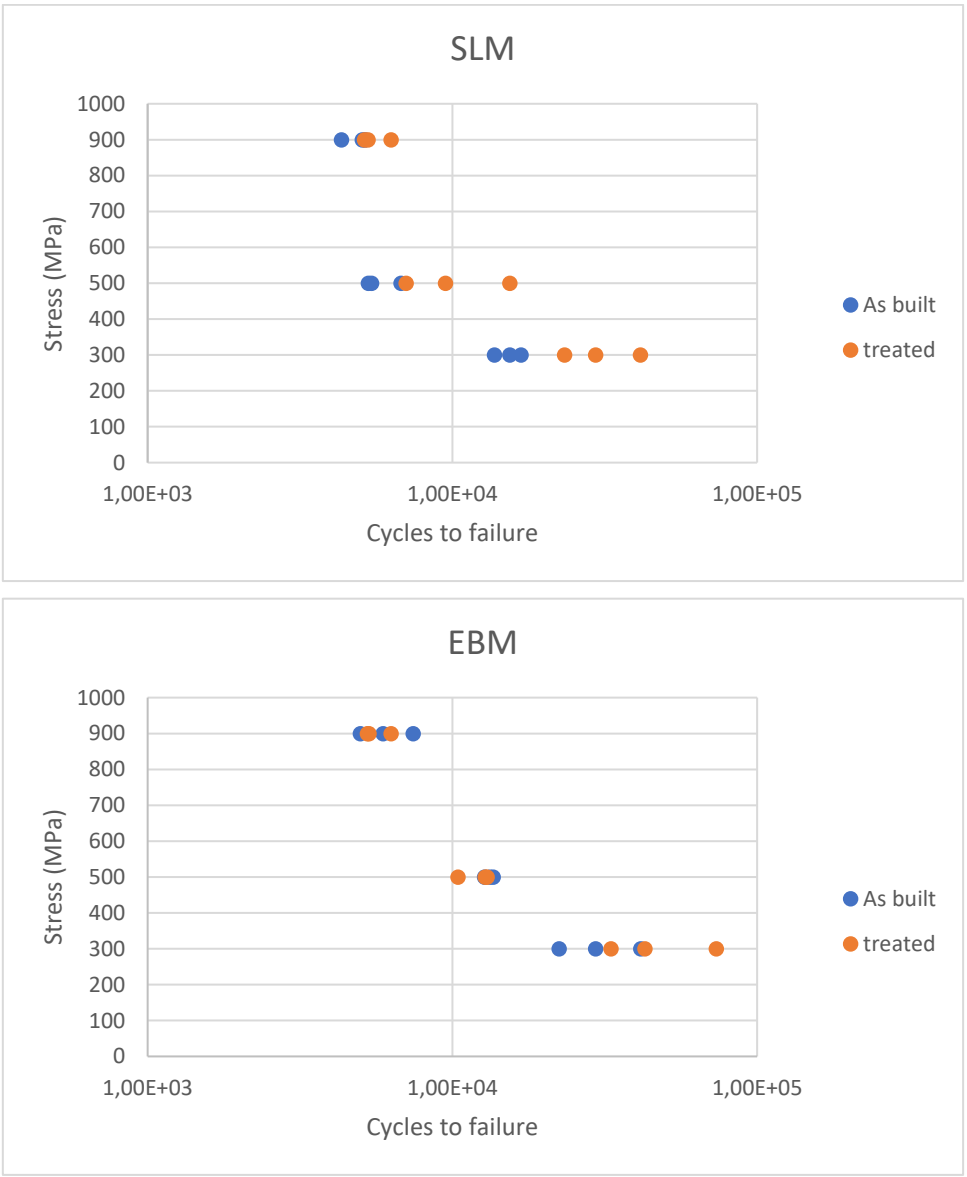


*Figure 38 SLM and EBM Whoeler curves, comparing as-built and treated case.*

For both cases, fatigue tests exhibit noticeable differences from the case of chemically machined EBM parts: while low cycle fatigue life is comparable, high cycle fatigue behavior is poor and none of the samples made it to reach $10^7$ cycles. In addition, while EBM samples tended to fail in the gauge length, the SLM samples were characterized by failure outside the gauge length, near the polished zone area.

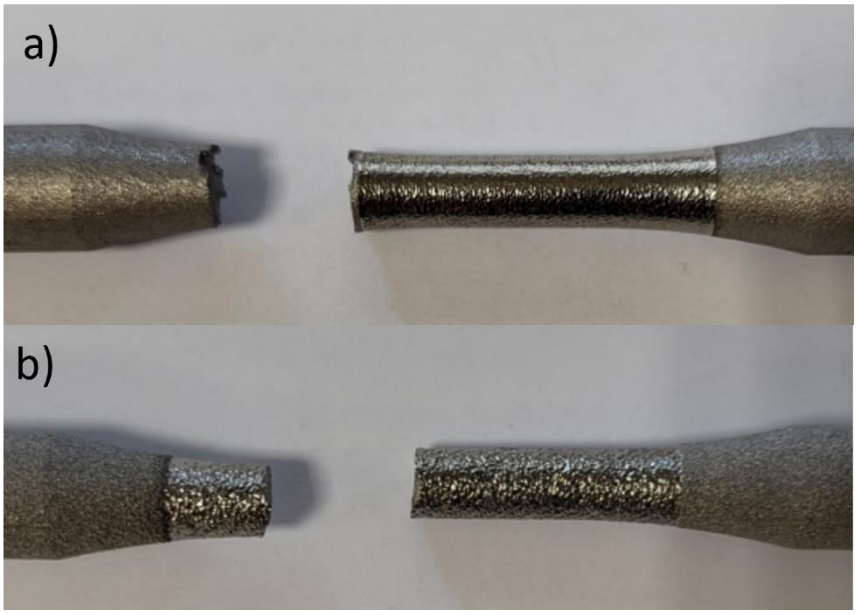


*Figure 39 a) SLM fractured sample; b) EBM fractured sample.*

In addition to fracture zone investigation, also the longitudinal section of these parts has been investigated to identify the reasons for the differences between the chemical treatment case and the ones between the SLM and EBM technologies themselves.

In Figures 40 and 41 an overview of the fracture surfaces for SLM and EBM samples is resumed respectively, the treated and untreated samples are compared at the same stress level.

In figure 42 and 43 the SLM and EBM longitudinal sections are shown, a combination of images taken with SEM and optical microscope highlight the internal defects and their differences.

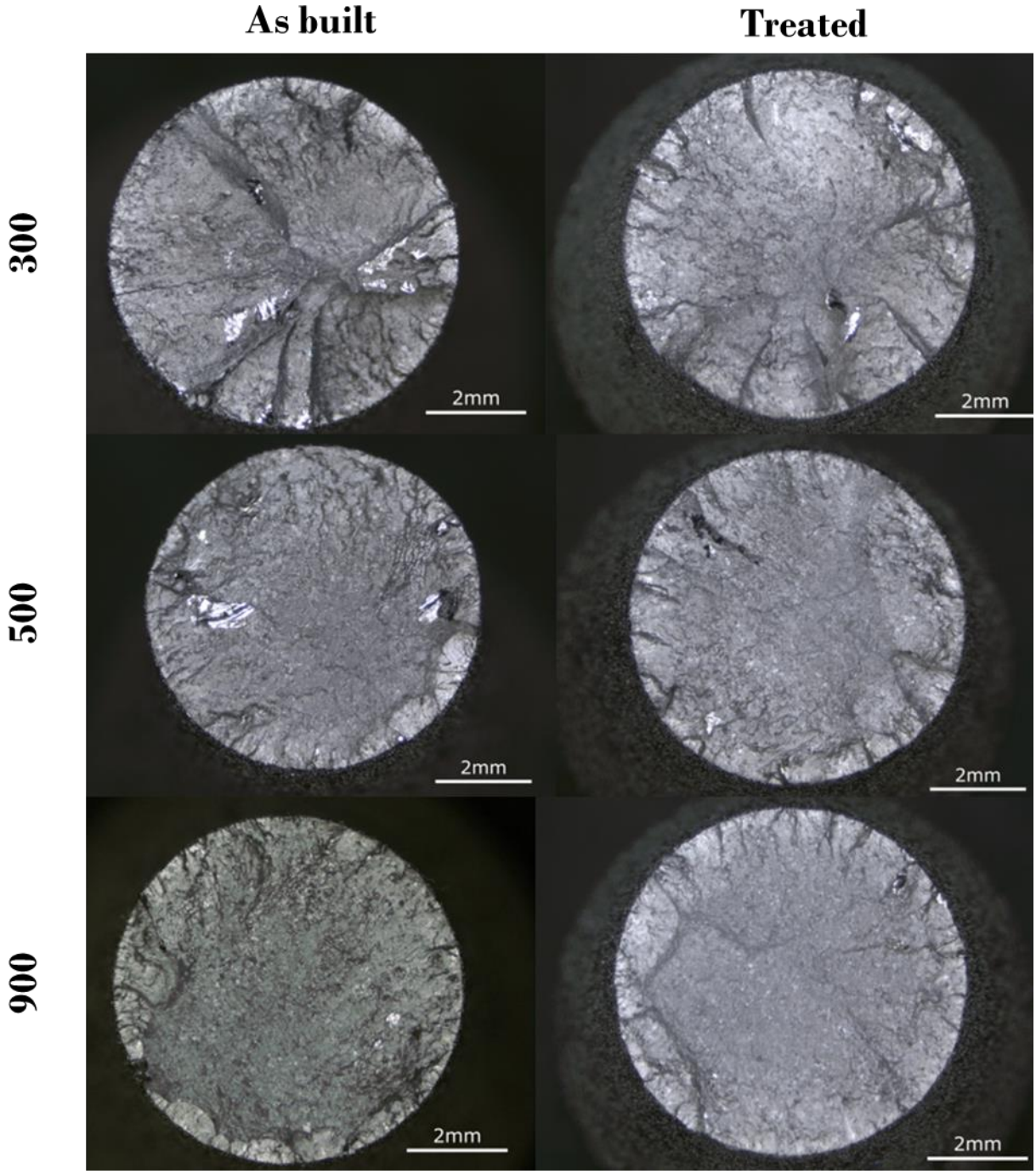


*Figure 40 SLM fracture surfaces: a comparison between untreated and treated samples, organized by the same stress level.*

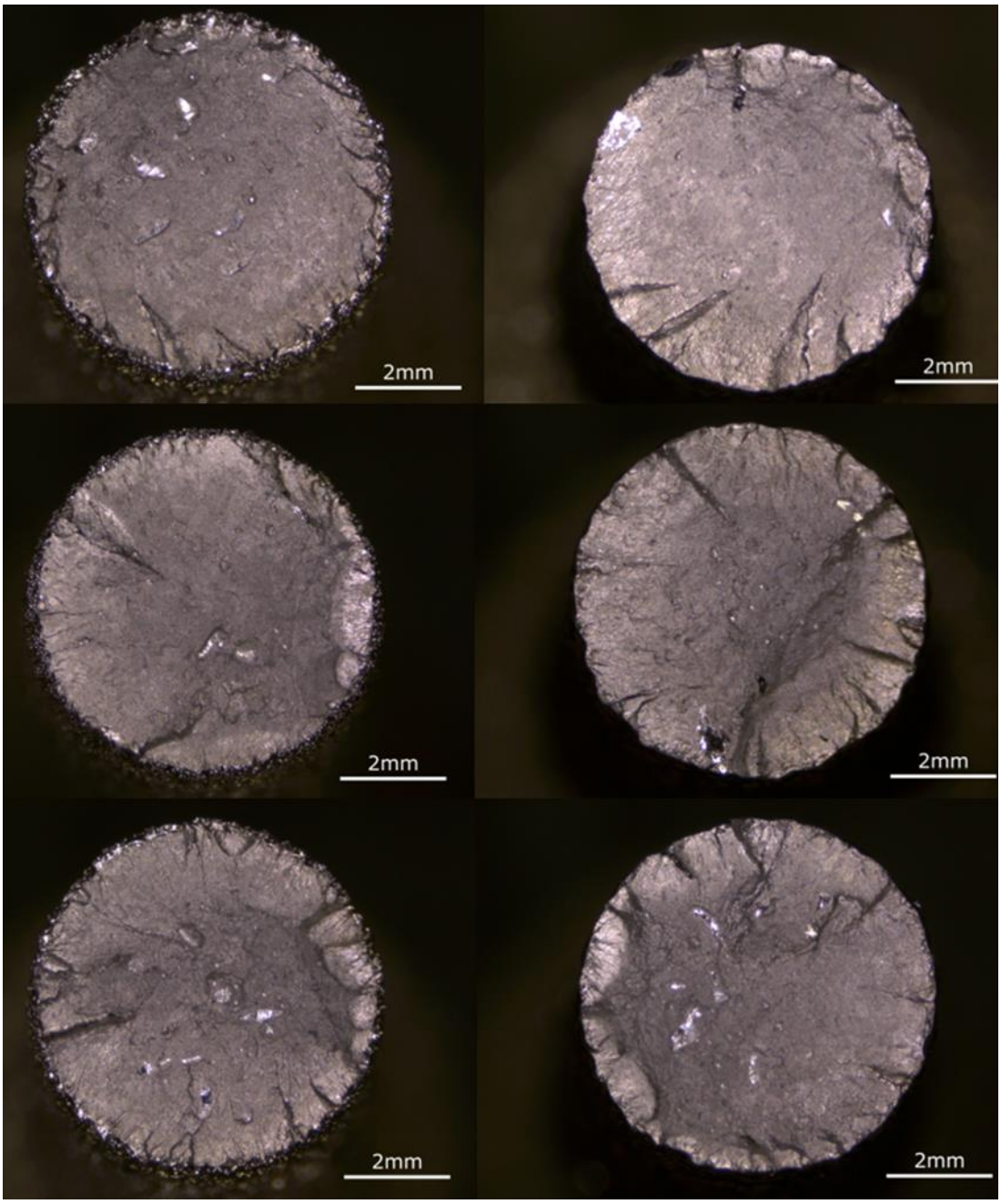


*Figure 41 EBM fracture surfaces: a comparison between untreated and treated samples, organized by the same stress level.*

Both cases are characterized by multiple cracks originating from the surface, the as built and treated fracture surfaces for SLM are identical because the fracture occurs outside the polished layer thus the cracking initiation system can be thought to be the same as the as built samples. Particularly, in the SLM case, the polished area fatigue properties are improved but it is not possible to identify the actual fatigue strength of the part. To address this issue, the polishing should be carried out also outside of the gauge length.

Regarding EBM samples, instead, the fracture is encouraging because it occurs properly in the gauge length. Looking at the fracture surface, a slight difference can be highlighted in the cracking system, however, the results from this analysis are quite different from the chemically machined samples: cracking on EBM laser polished parts is characterized by the presence of big cracks originating from multiple sites on the surface, in the chemical finishing case the cracking was less severe and cracks originated from single spots, generally pores.

With a longitudinal section of the samples, it can be possible to provide further details about these findings.

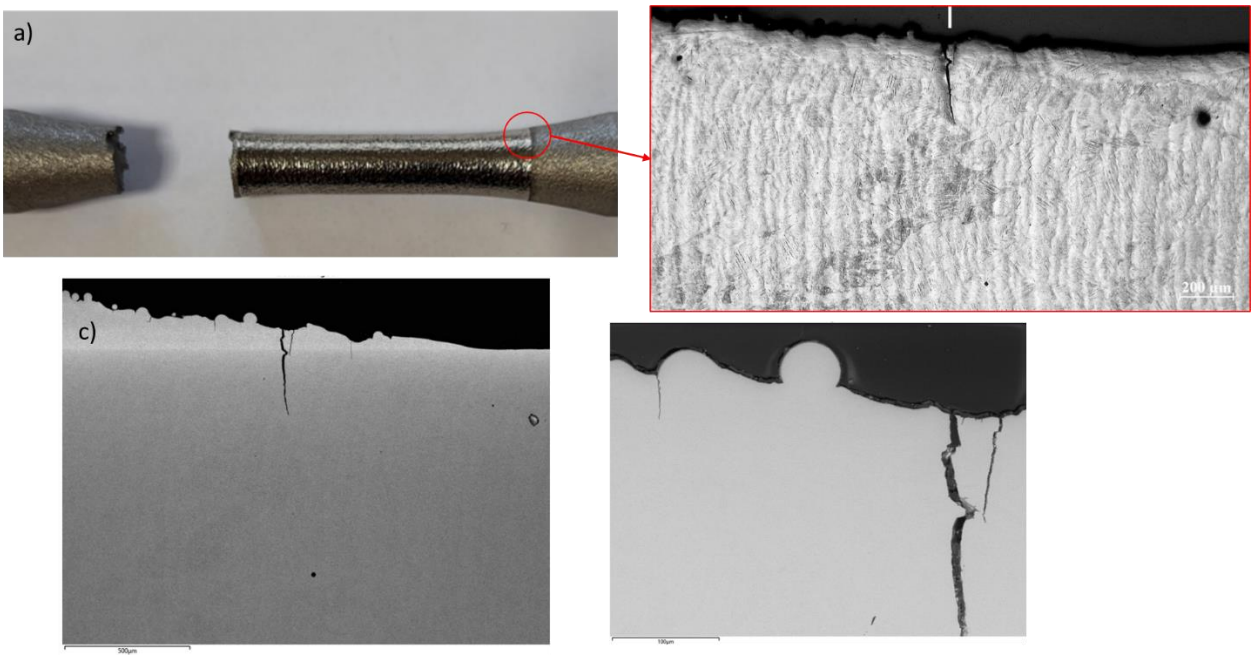


*Figure 42 a) Fractured SLM polished sample; b) closeup of the as built-polished interface taken with optical microscope; c) and d) details of the cracks identified in the previously mentioned zone.*

As shown in Figure 42, the as built-polished layer, despite the polishing being carried out also outside the minimal section area, is a preferential crack initiation site. In conclusion, the fatigue test on SLM polished samples are misleading since they are not referring to the polished area but to a portion of material that has a similar starting roughness as as-built samples but a bigger diameter, which is the reason behind the slight difference of Whoeler curves when comparing as built and treated samples.

A completely different cracking initiation mechanism can be identified for EBM polished samples, as shown in Figure 43.

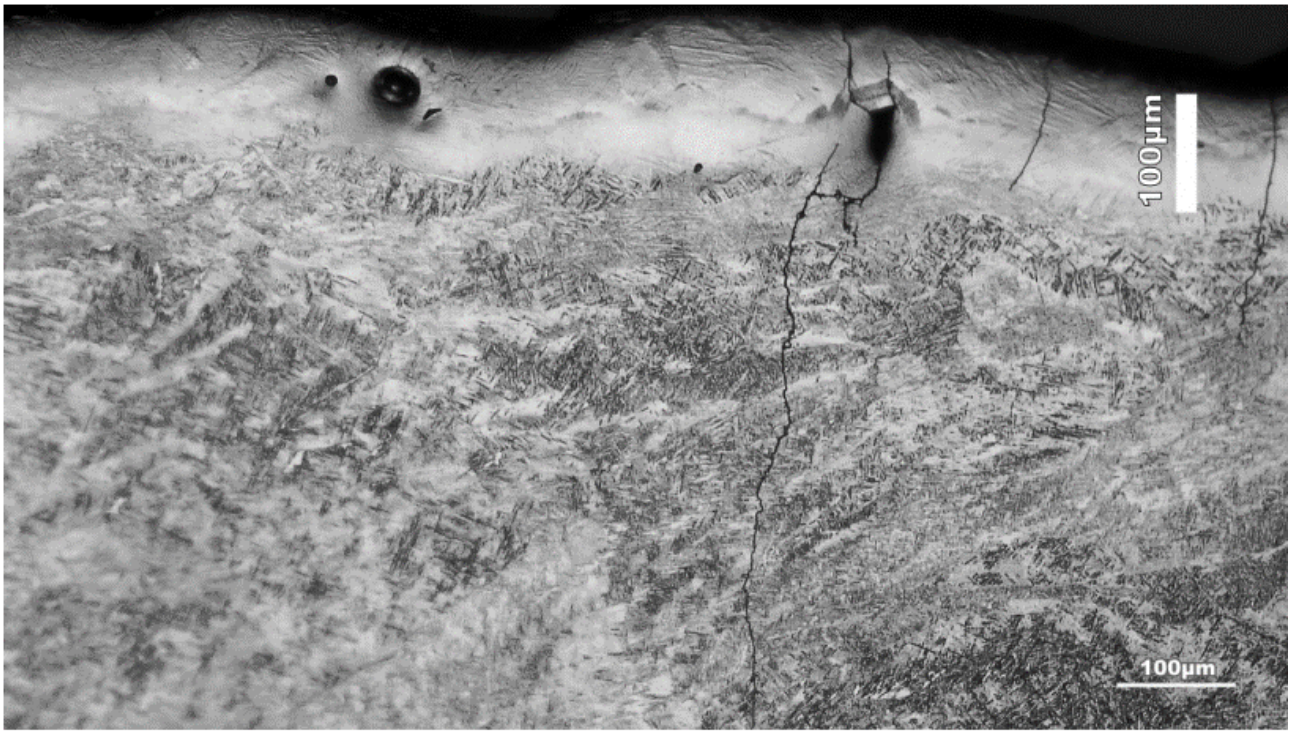


*Figure 43 polished area longitudinal section taken after fatigue testing.*

Laser polishing induces the presence of multiple defects, particularly gas inclusions and keyholes. This can be attributed to the severe heat-induced after four passes, which was the optimal parameter set to be chosen to polish the EBM starting surface. On one hand, the surface treatment required multiple passes to reduce the roughness significantly, on the other hand following Sa as a reference parameter to establish the best treatment proved wrong. It can be concluded that EBM samples fail properly on the polished area, differently from SLM samples, but failure occurs thanks to multiple induced preferential crack initiation sites in the polished layer, which results in a better fatigue behavior if compared to SLM polished samples but not if compared to chemically polished samples from the previous chapter.

## General conclusions

Considering the findings of this study, the following conclusions can be drawn:

1) Chemical machining has proven to be very effective in improving the surface quality of Ti6Al4V components made by EBM, and all the solutions used, with varying HF/HNO3 ratios, have proven to have smoothing capabilities. The addition of $HNO_3$ improves the final quality of the metal surface and the higher the $HNO_3$ concentration, the higher the reduction of the analyzed surface parameter. The smoothing process proceeds in two steps. In the first step, the unfused particles left on the surface are removed and in the second one, the characteristic sharp peaks are selectively dissolved. To achieve this result the transport properties of the solution play a key role, the viscosity increasing as the concentration of $HNO_3$ increases and consequently, the smoothing effect varies accordingly. In the absence of $HNO_3$, gaseous $H_2$ is produced on the metal surface, the gas bubbles acting as a barrier between the surface and solution with the consequence of a worse final quality and a lower ER. The process proceeds with an electrochemical mechanism in which the α phase is preferentially anodic and the β phase cathodic, with the consequence that the α phase is preferentially dissolved, leading to an impoverishment of Al on the metal surface. The addition of $HNO_3$ introduces a passivation stage in the dissolution process, and during this stage, a redistribution of ligands on the surface occurs mitigating partially the change in surface composition compared to the alloy in the bulk material.

2) Chemical machining is capable of improving the surface quality of cylindrical Ti6Al4V specimens produced by EBM. In the three analyzed conditions, roughness is considerably reduced, however, at the end of the treatment, the surface is characterized by predominant waviness. The waviness is not related to some fluid-dynamic effects since it develops also in stagnant conditions, it is, probably, related to the pre-existing layer-by-layer structure of the EBM samples. At high Reynolds numbers, the turbulence generates eddies that break the diffusion sublayer and increase the mass transfer rate. The eddies, also, enhance the selectivity towards the peaks of the surface.

3) Compared to untreated specimens, the fatigue behavior of treated specimens shows improved results, particularly in HCF. The negative effects of poor surface quality on

fatigue life are mitigated by chemical treatment, however, crack initiation is always associated with a surface/subsurface defect. The occurrence and size of defects can be reduced by improving the quality of the base material before treatment.

4) The laser polishing provided a more appreciable roughness reduction, analyzed through Sa, for the E-PBF case (68% for the best case) in comparison to the L-PBF one (52% for the best case). According to the quite high initial roughness of the as-built E-PBF specimens (54.3 ± 4.1 μm) against the L-PBF ones (10.2 ± 1.08 μm), this result was somehow expected considering the enhancement of the laser absorption when increasing the roughness of the surface under polishing. On the other hand, the very irregular surface morphology that implied the benefit highlighted in the previous point was also one of the major responsible for the weak correlation between the polishing parameters (specimen rotational speed, laser power, number of passes) and the roughness reduction for the E-PBF case, as proved by an adjusted R2 of the linear model of 0.17. This result was mainly ascribed to the high sensitivity of the re-melting ability of the laser against the surface unevenness. For both the E-PBF and L-PBF polishing experiments, no significant alteration of microstructure and chemical composition in the processed region was found.

5) While surface reduction results are encouraging, the polishing process shall be retailored to achieve better fatigue performances. Particularly:
- The polishing process must be carried out on the whole sample (clamping excluded) to avoid interfaces between polished and unpolished zones that can result in stress concentration. In addition, the unpolished zone triggers crack initiation, especially if it is located in a small diameter zone.
- The polishing process must be optimized taking into account also the polished layer quality, paying attention to the amount of heat transferred to avoid gas inclusions and keyholes. The treatment has a beneficial effect on surface quality but a detrimental effect on the sub-superficial area which is still critical for fatigue behavior.

As evidenced in points 1) to 3), the results on chemical machining are consistent and quite promising, as future directions the treatment application on complex geometry is one of the first targets for this research, to fully unlock the additive manufacturing free shape potential paired with a reliable surface treatment. On the other hand, it is necessary to

support this research phase with simulation to develop guidelines for starting geometries to make them suitable for chemical treatment: as the solution is selective towards peaky areas, the starting geometry should be different from the one intended at the end of the treatment. Regarding laser polishing, the issue reported in point 4) mainly affected the SLM samples but it probably didn't affect the EBM only because of the high amount of induced defects on the polished area. To address these two issues, the laser polishing treatment must take into account also the polished layer quality in terms of induced defects and microstructure. A new experimental campaign would be also required to polish the whole sample, taking into account new variables such as the fillet geometry and the laser polishing parameters in that zone since the geometry is not cylindrical. However, this first run highlighted interesting results and some guidelines for future developments of laser polishing for axisymmetric parts and particularly for fatigue testing/behavior.

# Bibliography


1. Scherillo F, Manco E, Hassanin A El, et al (2020) Chemical surface finishing of electron beam melted Ti6Al4V using HF-HNO3 solutions. J Manuf Process 60:400–409. https://doi.org/10.1016/j.jmapro.2020.10.033

2. Frazier WE (2014) Metal additive manufacturing: A review. J Mater Eng Perform 23:1917–1928. https://doi.org/10.1007/s11665-014-0958-z

3. Herzog D, Seyda V, Wycisk E, Emmelmann C (2016) Additive manufacturing of metals. Acta Mater 117:371–392. https://doi.org/10.1016/j.actamat.2016.07.019

4. Murr LE, Gaytan SM, Ramirez DA, et al (2012) Metal Fabrication by Additive Manufacturing Using Laser and Electron Beam Melting Technologies. J Mater Sci Technol 28:1–14. https://doi.org/10.1016/S1005-0302(12)60016-4

5. Wiberg A (2019) Towards Design Automation for Additive Manufacturing : A Multidisciplinary Optimization approach

6. Cabanettes F, Joubert A, Chardon G, et al (2018) Topography of as built surfaces generated in metal additive manufacturing: A multi scale analysis from form to roughness. Precis Eng 52:249–265. https://doi.org/https://doi.org/10.1016/j.precisioneng.2018.01.002

7. Liu S, Shin YC (2019) Additive manufacturing of Ti6Al4V alloy: A review. Mater Des 164:107552. https://doi.org/10.1016/j.matdes.2018.107552

8. Galati M, Iuliano L (2018) A literature review of powder-based electron beam melting focusing on numerical simulations. Addit Manuf 19:1–20. https://doi.org/https://doi.org/10.1016/j.addma.2017.11.001

9. Gisario A, Kazarian M, Martina F, Mehrpouya M (2019) Metal additive manufacturing in the commercial aviation industry: A review. J Manuf Syst 53:124–149. https://doi.org/https://doi.org/10.1016/j.jmsy.2019.08.005

10. Prisco U, Astarita A, El Hassanin A, Franchitti S (2019) Influence of processing parameters on microstructure and roughness of electron beam melted Ti-6Al-4V titanium alloy. Mater Manuf Process 34:1753–1760. https://doi.org/10.1080/10426914.2019.1683576

11. Brown CA, Hansen HN, Jiang XJ, et al (2018) Multiscale analyses and characterizations of surface topographies. CIRP Ann 67:839–862. https://doi.org/10.1016/j.cirp.2018.06.001

12. Borrelli R, Franchitti S, Pirozzi C, et al (2019) Ti6Al4V Parts Produced by Electron Beam

Melting: Analysis of Dimensional Accuracy and Surface Roughness. J Adv Manuf Syst 19:107–130. https://doi.org/10.1142/S0219686720500067

13. Rahmati S, Vahabli E (2015) Evaluation of analytical modeling for improvement of surface roughness of FDM test part using measurement results. Int J Adv Manuf Technol 79:823–829. https://doi.org/10.1007/s00170-015-6879-7

14. Tolochko NK, Mozzharov SE, Yadroitsev IA, et al (2004) Balling processes during selective laser treatment of powders. Rapid Prototyp J 10:78–87. https://doi.org/10.1108/13552540410526953

15. Du W, Bai Q, Zhang B (2016) A Novel Method for Additive/Subtractive Hybrid Manufacturing of Metallic Parts. Procedia Manuf 5:1018–1030. https://doi.org/10.1016/j.promfg.2016.08.067

16. Maamoun AH, Elbestawi MA, Veldhuis SC (2018) Influence of Shot Peening on AlSi10Mg Parts Fabricated by Additive Manufacturing. J Manuf Mater Process 2:. https://doi.org/10.3390/jmmp2030040

17. AlMangour B, Yang J-M (2016) Improving the surface quality and mechanical properties by shot-peening of 17-4 stainless steel fabricated by additive manufacturing. Mater Des 110:914–924. https://doi.org/https://doi.org/10.1016/j.matdes.2016.08.037

18. Bernevig-Sava MA, Stamate C, Lohan NM, et al (2019) Considerations on the surface roughness of SLM processed metal parts and the effects of subsequent sandblasting. IOP Conf Ser Mater Sci Eng 572:. https://doi.org/10.1088/1757-899X/572/1/012071

19. Barletta M (2009) Progress in abrasive fluidized bed machining. J Mater Process Technol 209:6087–6102. https://doi.org/10.1016/j.jmatprotec.2009.04.009

20. Atzeni E, Barletta M, Calignano F, et al (2016) Abrasive Fluidized Bed (AFB) finishing of AlSi10Mg substrates manufactured by Direct Metal Laser Sintering (DMLS). Addit Manuf 10:15–23. https://doi.org/https://doi.org/10.1016/j.addma.2016.01.005

21. Nagalingam AP, Yuvaraj HK, Yeo SH (2020) Synergistic effects in hydrodynamic cavitation abrasive finishing for internal surface-finish enhancement of additive-manufactured components. Addit Manuf 33:101110. https://doi.org/https://doi.org/10.1016/j.addma.2020.101110

22. Zhang X, Chen L (2020) Effects of laser scanning speed on surface roughness and mechanical properties of aluminum/Polylactic Acid (Al/PLA) composites parts fabricated by fused deposition modeling. Polym Test 91:106785. https://doi.org/10.1016/j.polymertesting.2020.106785

23. Yung KC, Xiao TY, Choy HS, et al (2018) Laser polishing of additive manufactured CoCr alloy components with complex surface geometry. J Mater Process Technol 262:53–64.

https://doi.org/10.1016/j.jmatprotec.2018.06.019

24. Chen X hui, Chen B, Cheng X, et al (2020) Microstructure and properties of hybrid additive manufacturing 316L component by directed energy deposition and laser remelting. J Iron Steel Res Int 27:842–848. https://doi.org/10.1007/s42243-020-00396-y

25. Obeidi MA, Mussatto A, Dogu MN, et al (2022) Laser surface polishing of Ti-6Al-4V parts manufactured by laser powder bed fusion. Surf Coatings Technol 434:128179. https://doi.org/10.1016/j.surfcoat.2022.128179

26. Obeidi MA, McCarthy E, O'Connell B, et al (2019) Laser polishing of additive manufactured 316L stainless steel synthesized by selective laser melting. Materials (Basel) 12:. https://doi.org/10.3390/ma12060991

27. Obeidi M, Mccarthy E, Ubani S, et al (2019) Effect of Surface Roughness on CO2 Laser Absorption by 316L Stainless Steel and Aluminum. Mater Perform Charact 8:20180091. https://doi.org/10.1520/MPC20180091

28. Ahmed Obeidi M, McCarthy E, Brabazon D (2016) Methodology of laser processing for precise control of surface micro-topology. Surf Coatings Technol 307:702–712. https://doi.org/10.1016/j.surfcoat.2016.09.075

29. Manco E, Cozzolino E, Astarita A (2022) Laser polishing of additively manufactured metal parts : a review. Surf Eng 1–17. https://doi.org/10.1080/02670844.2022.2072080

30. Scherillo F (2019) Chemical surface finishing of AlSi10Mg components made by additive manufacturing. Manuf Lett 19:5–9. https://doi.org/https://doi.org/10.1016/j.mfglet.2018.12.002

31. Wysocki B, Idaszek J, Buhagiar J, et al (2019) The influence of chemical polishing of titanium scaffolds on their mechanical strength and in-vitro cell response. Mater Sci Eng C 95:428–439. https://doi.org/https://doi.org/10.1016/j.msec.2018.04.019

32. Kobryn PA, Semiatin SL (2001) Mechanical Properties of Laser-Deposited Ti-6Al-4V P.A. Kobryn and S.L. Semiatin Air Force Research Laboratory, AFRL/MLLMP, Wright-Patterson Air Force Base, OH 45433-7817. Int Solid Free Fabr Symp 179–186

33. Mower TM, Long MJ (2016) Mechanical behavior of additive manufactured, powder-bed laser-fused materials. Mater Sci Eng A 651:198–213. https://doi.org/10.1016/j.msea.2015.10.068

34. Fatemi A, Molaei R, Simsiriwong J, et al (2019) Fatigue behaviour of additive manufactured materials: An overview of some recent experimental studies on Ti-6Al-4V considering various processing and loading direction effects. Fatigue Fract Eng Mater Struct 42:991–1009.

https://doi.org/10.1111/ffe.13000

35. Hassan T, Liu Z (2001) On the difference of fatigue strengths from rotating bending, four-point bending, and cantilever bending tests. Int J Press Vessel Pip 78:19–30. https://doi.org/10.1016/S0308-0161(00)00080-6

36. Gockel J, Sheridan L, Koerper B, Whip B (2019) The influence of additive manufacturing processing parameters on surface roughness and fatigue life. Int J Fatigue 124:380–388. https://doi.org/https://doi.org/10.1016/j.ijfatigue.2019.03.025

37. Yadollahi A, Shamsaei N (2017) Additive manufacturing of fatigue resistant materials: Challenges and opportunities. Int J Fatigue 98:14–31. https://doi.org/https://doi.org/10.1016/j.ijfatigue.2017.01.001

38. Cutolo A, Elangeswaran C, Muralidharan GK, Van Hooreweder B (2022) On the role of building orientation and surface post-processes on the fatigue life of Ti-6Al-4V coupons manufactured by laser powder bed fusion. Mater Sci Eng A 840:142747. https://doi.org/https://doi.org/10.1016/j.msea.2022.142747

39. Croccolo D, De Agostinis M, Fini S, et al (2016) Influence of the build orientation on the fatigue strength of EOS maraging steel produced by additive metal machine. Fatigue Fract Eng Mater Struct 39:637–647. https://doi.org/10.1111/ffe.12395

40. Nezhadfar PD, Shrestha R, Phan N, Shamsaei N (2019) Fatigue behavior of additively manufactured 17-4 PH stainless steel: Synergistic effects of surface roughness and heat treatment. Int J Fatigue 124:188–204. https://doi.org/https://doi.org/10.1016/j.ijfatigue.2019.02.039

41. Tridello A, Fiocchi J, Biffi CA, et al (2019) VHCF response of Gaussian SLM AlSi10Mg specimens: Effect of a stress relief heat treatment. Int J Fatigue 124:435–443. https://doi.org/https://doi.org/10.1016/j.ijfatigue.2019.02.020

42. Beevers E, Brandão AD, Gumpinger J, et al (2018) Fatigue properties and material characteristics of additively manufactured AlSi10Mg – Effect of the contour parameter on the microstructure, density, residual stress, roughness and mechanical properties. Int J Fatigue 117:148–162. https://doi.org/https://doi.org/10.1016/j.ijfatigue.2018.08.023

43. Blateyron F (2013) The Areal Field Parameters. In: Characterisation of Areal Surface Texture. pp 15–43

44. Sutter EMM, Goetz-Grandmont GJ (1990) The behaviour of titanium in nitric-hydrofluoric acid solutions. Corros Sci 30:461–476. https://doi.org/https://doi.org/10.1016/0010-938X(90)90051-6

45. Sutter EMM, Hlawka F, Cornet A (1990) Comparative Behavior of Titanium and Zirconium in Hydrofluoric-Nitric Acid Pickling Solutions. Corrosion 46:537–544. https://doi.org/10.5006/1.3585144

46. Chatterjee B (1984) Chemical brightening of aluminium. Mater Chem Phys. https://doi.org/10.1016/0254-0584(84)90096-8

47. Branch LC (1998) Bright dipping aluminum. Met Finish 96:24–29. https://doi.org/https://doi.org/10.1016/S0026-0576(98)81273-7

48. Evgeny B, Hughes T, Eskin D (2016) Effect of surface roughness on corrosion behaviour of low carbon steel in inhibited 4 M hydrochloric acid under laminar and turbulent flow conditions. Corros Sci 103:196–205. https://doi.org/10.1016/j.corsci.2015.11.019

49. (1961) Transport phenomena, R. B. Bird, W. E. Stewart, and E. N. Lightfoot, John Wiley and Sons, Inc., New York (1960). 780 pages. $11.50. AIChE J 7:5J-6J. https://doi.org/https://doi.org/10.1002/aic.690070245

50. Franchitti S, Pirozzi C, Borrelli R (2020) Influence of hot isostatic pressing and surface finish on the mechanical behaviour of Ti6Al4V processed by electron beam melting. Fatigue Fract Eng Mater Struct 43:2828–2841. https://doi.org/10.1111/ffe.13295

51. Manco E, Scherillo F, Guerrera C, et al (2023) Influence of chemical machining on axial fatigue behaviour of electron beam melted Ti6Al4V parts. Manuf Lett 35:6–10. https://doi.org/10.1016/j.mfglet.2022.11.001

52. Carrion PE, Shamsaei N, Daniewicz SR, Moser RD (2017) Fatigue behavior of Ti-6Al-4V ELI including mean stress effects. Int J Fatigue 99:87–100. https://doi.org/10.1016/j.ijfatigue.2017.02.013

53. Chern AH, Nandwana P, Yuan T, et al (2019) A review on the fatigue behavior of Ti-6Al-4V fabricated by electron beam melting additive manufacturing. Int J Fatigue 119:173–184. https://doi.org/https://doi.org/10.1016/j.ijfatigue.2018.09.022

54. Kahlin M, Ansell H, Moverare JJ (2017) Fatigue behaviour of notched additive manufactured Ti6Al4V with as-built surfaces. Int J Fatigue 101:51–60. https://doi.org/https://doi.org/10.1016/j.ijfatigue.2017.04.009

55. Greitemeier D, Donne CD, Syassen F, et al (2016) Effect of surface roughness on fatigue performance of additive manufactured Ti–6Al–4V. Mater Sci Technol 32:629–634. https://doi.org/10.1179/1743284715Y.0000000053

56. Chowdhury S, Yadaiah N, Prakash C, et al (2022) Laser powder bed fusion: a state-of-the-art review of the technology, materials, properties & defects, and numerical modelling. J Mater Res Technol 20:2109–2172. https://doi.org/https://doi.org/10.1016/j.jmrt.2022.07.121

57. Chen L, Richter B, Zhang X, et al (2021) Effect of laser polishing on the microstructure and mechanical properties of stainless steel 316L fabricated by laser powder bed fusion. Mater Sci Eng A 802:140579. https://doi.org/10.1016/j.msea.2020.140579

58. Calignano F (2018) Investigation of the accuracy and roughness in the laser powder bed fusion process. Virtual Phys Prototyp 13:1–8. https://doi.org/10.1080/17452759.2018.1426368

59. El Hassanin A, Obeidi MA, Scherillo F, Brabazon D (2021) CO2 laser polishing of laser-powder bed fusion produced AlSi10Mg parts. Surf Coatings Technol 419:127291. https://doi.org/10.1016/j.surfcoat.2021.127291